

Sequential estimation of disturbed aerodynamic flows from sparse measurements via a reduced latent space

Hanieh Mousavi^{1,*}, Anya Jones¹, and Jeff Eldredge¹

¹Mechanical and Aerospace Engineering, University of California, Los Angeles, Los Angeles, CA 90095-1597, USA

*Corresponding author, email: hnmousavi@ucla.edu

Abstract

This work presents a fast, scalable, and uncertainty-aware methodology suitable for real-time estimation of key aerodynamic states—including instantaneous vorticity fields and aerodynamic loads—during severe gust encounters, where strong flow separation and vortex–gust interactions dominate the dynamics. The methodology, trained and tested on high-fidelity simulations of two-dimensional wing–gust encounters and corresponding sparse pressure data, combines the strengths of physics-based ensemble filtering with data-driven surrogate modeling in a learned low-order space. Within this reduced space, latent dynamics and sensor observation operators are learned using neural networks, enabling efficient and expressive modeling of complex aerodynamic responses. These data-driven components are then embedded within a low-rank Ensemble Kalman Filter (LREnKF), yielding a computationally efficient scheme that combines data-driven expressivity with physical interpretability in the original high-dimensional space. Because assimilation occurs entirely within the learned reduced space, the updates are fast enough for real-time use in flight applications, ensuring that aerodynamic states can be continuously estimated from streaming pressure data. The filtering process corrects the predicted states predominantly in directions that are both dynamically significant and observable, as determined by the dominant modes of the learned observation operator. This targeted correction mechanism improves filter efficiency and mitigates the risk of over- or under-adjusting state variables in unobservable or weakly constrained subspaces. An analysis of the observability reveals how sensor informativeness evolves over time, particularly during wing–gust interactions. The framework readily accounts for sensor failure, and sensor dropout experiments show that LREnKF adaptively re-weights neighboring sensors to compensate for lost information, preserving estimation quality even under degraded sensing configurations.

1 Introduction

Aerial disturbances, particularly those arising from various gust encounters, frequently disrupt the nominal operation and controlled maneuvering of small air vehicles. In gust-passage scenarios, the disturbance acts over a limited time window, creating sharp, transient deviations in the flow field that are especially difficult to detect and predict in real time. These disruptions can be mitigated through active control strategies—such as linear feedback control or reinforcement learning (RL)—that enable the system to respond adaptively. However, effective active control requires real-time access to the underlying states of the dynamical system to detect anomalies and take corrective action. In aerodynamic applications, these states are typically not directly measurable. Instead, transient flow variations are reflected in (and partially observable through) the sensors, such as pressure taps mounted on the wings. These measurements serve as indirect observables that can be sequentially assimilated to infer the hidden flow states. Without a good initial guess, it is impossible to infer the inherently high-dimensional flow field from a single measurement taken from a limited number of sensors. Though sequential filters, such as those at the heart of this work, leverage past measurements and dynamical predictions to progressively narrow the search region, each measurement update of the state is still heavily challenged to navigate the high-dimensional space.

To address this challenge, a low-dimensional state space can be constructed to serve as a compressed representation of the full flow field, describing only the most energetic structures and essential physics. Traditional approaches rely on linear projection techniques, such as Proper Orthogonal Decomposition

(POD) (Berkooz et al. 1993) and Dynamic Mode Decomposition (DMD) (Schmid 2010), which approximate the system in terms of dominant linear modes. However, these methods have been shown to be inadequate for strongly nonlinear systems—such as gust-disturbed flows—where the underlying dynamics often evolve on a nonlinear manifold (Fukami and Taira 2023). In such settings, the modes excluded by linear truncation can significantly affect the system’s evolution (Maulik et al. 2020). To overcome this limitation, nonlinear data compression techniques based on deep learning (DL)—such as standard autoencoders (Fukami and Taira 2023, Xie et al. 2024, Mousavi and Eldredge 2025) and their variational counterparts (VAEs) (Fraccaro et al. 2017, He et al. 2025)—have gained traction for their ability to learn compact, task-specific latent representations that better capture the transient dynamics of complex systems.

Once a reduced-order latent space is learned, data assimilation (DA) can be performed efficiently within this space to enable real-time state estimation with low computational overhead using sequential filtering. From the estimated latent state and its uncertainty, the corresponding estimates in the full flow field state space can be reconstructed via the decoder. Typically, filtering frameworks involve two critical components to evolve the probability distribution of states: a *forecast operator* that propagates states forward in time, and an *observation operator* that maps states to measurable outputs, enabling state correction based on new observations (Asch et al. 2016, Eldredge and Mousavi 2025). In a reduced space, these operators can be approximated by DL-based surrogate models, providing a tractable alternative to traditional high-fidelity solvers (Bach et al. 2024). With the abundance of data, neural networks (NNs), in particular, are well-suited for this task as they are differentiable and can either augment or fully replace physics-based models in scenarios where simulations are expensive or unavailable (Jin et al. 2021).

Several recent works have demonstrated the successful use of NNs for learning surrogate models. For instance, Fraccaro et al. (2017) developed the Kalman Variational Autoencoder (Kalman-VAE), which uses a recurrent neural network (RNN) to model latent dynamics from partially observed image sequences. Maulik et al. (2020) employed long short-term memory (LSTM) networks to model the evolution of unresolved POD modes in turbulent flows. In a Kalman filtering setting, Coskun et al. (2017) used three separate LSTM models to jointly learn the latent dynamics and the associated process and measurement noise statistics. Other works embed physical constraints into the learned latent dynamics: Popov and Sandu (2022) and He et al. (2025) constructed physics-informed surrogate models constrained by PDE structure. The sequence prediction models employed in the foregoing references leverage the full temporal history to forecast future states, often using RNNs with memory kernels (Tang et al. 2020, Cheng et al. 2022).

Despite their effectiveness, memory-based models violate the foundational Markov assumption in filtering, which posits that system evolution depends only on the current states (Maybeck 1982). To preserve this assumption, Neural Ordinary Differential Equations (Neural ODEs) have emerged as a promising alternative. Neural ODEs define continuous-time latent dynamics via:

$$\frac{dx}{dt} = f_{\theta}(x) \quad (1)$$

where $f_{\theta}(x)$ is a NN parameterized by θ . Unlike RNNs, Neural ODEs inherently model Markovian transitions, making them particularly compatible with sequential filtering architectures.

Building on this foundation, several studies have integrated DL techniques into traditional filtering frameworks for improved state estimation. Jouaber et al. (2021) introduced a neural Kalman filter in which an LSTM dynamically learns the process noise covariance, with the full Kalman update embedded in the computational graph. Song et al. (2022) proposed KFFLSTM, a hybrid architecture that jointly learns dynamics and noise models using LSTMs, though it departs from the Markovian assumption. Revach et al. (2022) developed KalmanNet, which learns the Kalman gain in extended Kalman filtering with known models but unknown noise statistics, albeit without explicit uncertainty quantification. In large-scale geophysical applications, Wang and Shen (2024) used NNs to enhance ensemble adjustment Kalman filters for strongly coupled ocean–atmosphere systems, and Howard et al. (2024) developed a CNN-based surrogate to accelerate the Ensemble Kalman Filter (EnKF) analysis step in high-resolution observational settings. Besides model-based filtering, fully model-free Bayesian estimators have also been introduced: Ghosh et al. (2024b) proposed DANSE, an RNN-based Bayesian filter that infers posterior distributions from noisy observations, and Ghosh et al. (2024a) extended it to a semi-supervised version, SemiDANSE, incorporating state supervision as a regularization term. A recent line of work (Özalp et al. 2025) has addressed DA by coupling convolutional autoencoders with recurrent latent models and ensemble Kalman filtering, resulting in the DA-CAE-ESN framework for chaotic flows such as

Kuramoto–Sivashinsky and Kolmogorov turbulence. Beyond filtering, variational DA approaches like 3D-Var and 4D-Var remain widely used for deterministic state estimation via optimization of forecast-observation mismatches (Le Dimet and Talagrand 1986, Kalnay 2003, de Rosnay et al. 2022, Bach et al. 2024). However, these methods only yield point estimates and lack real-time adaptability, making them unsuitable for control-driven aerodynamic applications requiring fast and probabilistic updates.

This work introduces a data assimilation algorithm for unsteady fluid flows in a reduced-dimensional latent space. The framework we present provides real-time flow state estimation in aerodynamic environments with strong transient disturbances, observed only with sparse and noisy surface pressure measurements. While our prior work (Mousavi and Eldredge 2025) explored the inference of the latent state and its uncertainty from sparse, noisy measurements, it considered this inference only as a single instantaneous task and did not leverage the evolving state estimate from past observations. The present study fills this gap by embedding DA within a learned latent space, enabling sequential state estimation conditioned on the full history of observations. The framework employs a nonlinear physics-augmented autoencoder to extract a compact latent representation of the high-dimensional vorticity field. The latent state is updated in time using sequential filtering, in which both the forecast and observation operators are learned via neural networks and incorporated into the low-rank ensemble Kalman filter (LREnKF) introduced by Le Provost et al. (2022). Unlike the DA-CAE-ESN framework of Özalp et al. (2025), which was demonstrated on canonical chaotic flows through augmented reservoir state and reported limited estimation accuracy even with sixteen sensors, our method is specifically designed for aerodynamic gust encounters and achieves robust reconstructions from substantially fewer measurements. Through the LREnKF formulation used in this study, updates are restricted to measurement-informative latent directions, enabling efficient use of very sparse sensing. Thus, this integration of the low-dimensional latent space with a structured sequential estimator ensures both computational efficiency and physical interpretability in the uncertainty-aware estimation of the evolving aerodynamic state under gust-induced disturbances.

The paper is organized as follows: Section 2 formulates the problem and outlines the mathematical framework that underpins our study. Section 3 reports results on complex, transient, disturbance-driven aerodynamic cases, demonstrating efficient online state estimation with the approach. Finally, Section 4 summarizes the main findings and discusses limitations, directions, and suggestions for future work.

2 Problem description and methodology

In this study, we present a unified framework that integrates data-driven modeling with sequential estimation to reconstruct unsteady flow fields and aerodynamic loads from sparse, noisy surface pressure measurements. The central aim is to enable fast, robust, and uncertainty-aware inference under strongly disturbed conditions, where traditional simulation or filtering approaches become computationally prohibitive or inaccurate. Figure 1 illustrates the overall concept. At the heart of the framework is a compact latent space, ξ , learned through nonlinear compression techniques based on DL. This reduced representation captures the essential flow physics while filtering out redundancy, thereby providing a tractable foundation for data assimilation. Surrogate dynamical and observation models—required by DA task—are then trained directly in this latent space. During inference, new surface pressure data are assimilated with the LREnKF, which updates the latent state distribution efficiently by exploiting measurement-informative subspaces. Finally, the updated latent samples are decoded back into the physical space, yielding flow-field reconstructions and load estimates along with their associated uncertainties.

2.1 Problem statement

We need data for DL tasks. To generate training and testing data, we simulate an unsteady, incompressible two-dimensional flow over a NACA 0012 airfoil at angles of attack (AoA) $\alpha \in \{20^\circ, 30^\circ, 40^\circ, 50^\circ, 60^\circ\}$. The undisturbed flow is characterized by a chord-based Reynolds number of $\text{Re} = U_\infty c / \nu = 100$, where U_∞ is the freestream velocity, c is the chord length, and ν is the kinematic viscosity of the fluid. To model disturbed conditions, we introduce localized gusts upstream of the airfoil at randomly selected instants during the natural vortex shedding cycle of the airfoil. These gusts are implemented as a body force \mathbf{F} —Gaussian distributed in space and time, and applied to the flow field—defined as:

$$\mathbf{F}(x, y, t) = \rho U_\infty c^2 \frac{(D_x, D_y)}{\pi^{3/2} \sigma_x \sigma_y \sigma_t} \exp \left[-\frac{(x - x_o)^2}{\sigma_x^2} - \frac{(y - y_o)^2}{\sigma_y^2} - \frac{(t - t_o)^2}{\sigma_t^2} \right], \quad (2)$$

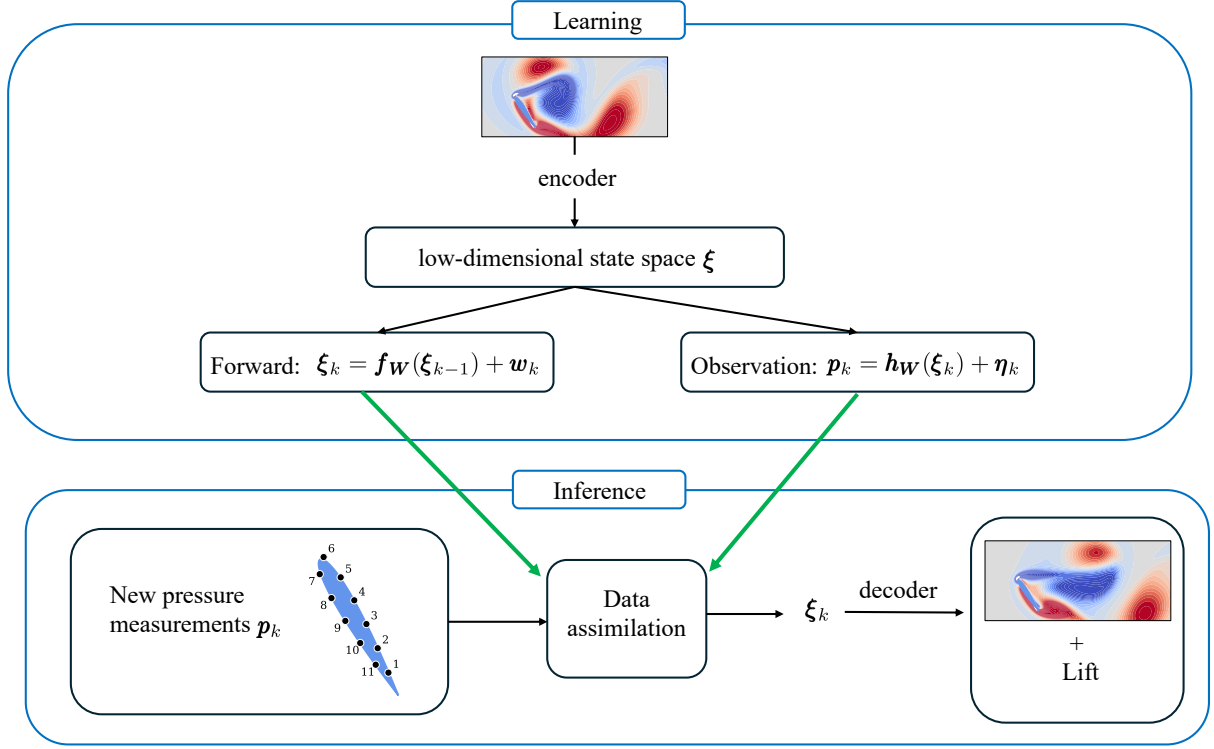


Figure 1: Block diagram summarizing the framework developed and applied in this study.

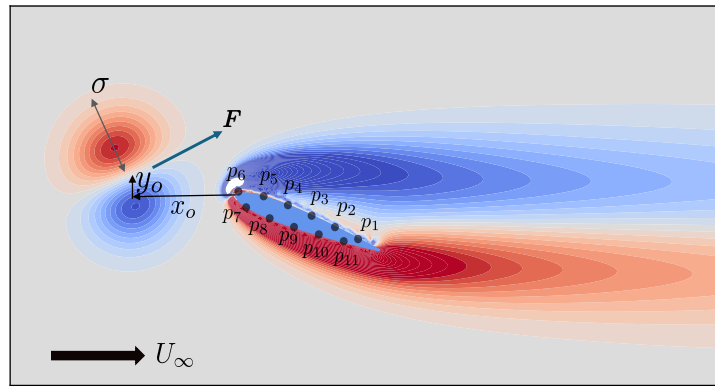


Figure 2: Configuration of the problem, illustrating the relative position of the gust centre with respect to the leading edge of the airfoil, the size of the Gaussian disturbance and the indices of sensors mounted on the airfoil.

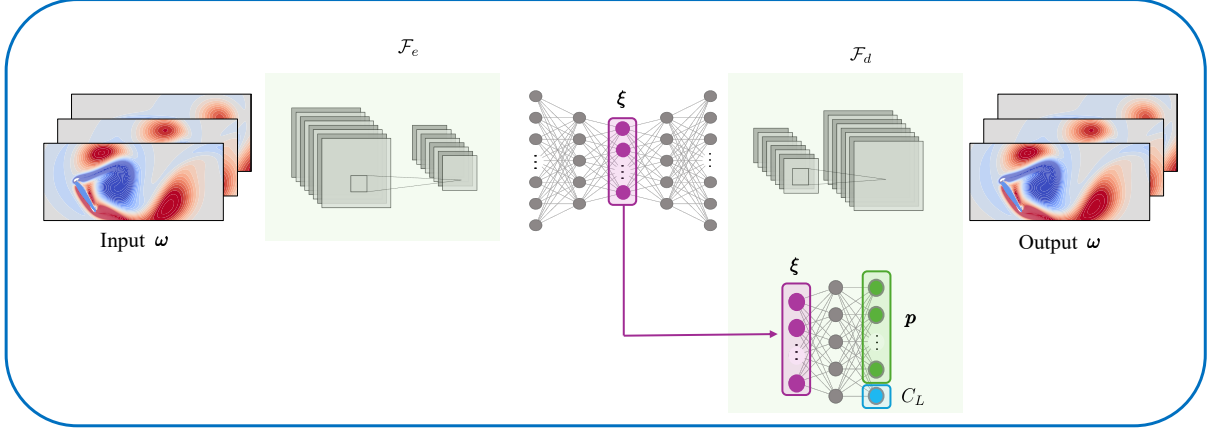


Figure 3: Network architecture in the present study, including a non-linear physics-augmented autoencoder. The observation operator that maps the learned latent vector to the pressure measurements is learned on-the-fly while training the autoencoder.

where ρ is the fluid density, (D_x, D_y) are the dimensionless forcing amplitudes in the streamwise and transverse directions, σ_x and σ_y are the spatial spreads of the forcing field, and σ_t is its temporal width. The gust center is located at (x_o, y_o) relative to the leading edge of the airfoil and introduced at time t_o . The schematic of the problem configuration is illustrated in figure 2. In all simulations, we fix $D_x = 2.0$, $x_o = -0.8c$, while other gust parameters are randomly sampled from the ranges $D_y \in [-2.0, 2.0]$, $\sigma_x = \sigma_y = \sigma \in [0.05c, 0.2c]$, $y_o \in [-0.25c, 0.25c]$, and $t_o \in [0.3c/U_\infty, 5.0c/U_\infty]$. The upper bound for t_o is intentionally selected near the vortex shedding period to ensure gusts interact with the airfoil at various phases within the first cycle. In this study, Latin Hypercube Sampling is employed to efficiently generate diverse combinations of gust parameters across the high-dimensional design space. This stratified sampling approach ensures uniform coverage of the parameter ranges while minimizing the total number of simulations required for training and evaluation.

The direct numerical simulation of the incompressible Navier–Stokes equations is performed in vorticity–streamfunction form using the Lattice Green’s Function/Immersed Layers method developed by Eldredge (2022). This approach enables high-resolution flow computation within a relatively compact domain, made possible by the efficient treatment of boundary conditions via the lattice Green’s function. The simulations are conducted over a Cartesian domain spanning $(-2c, 4c) \times (-2c, 2c)$ in the x and y directions, respectively, with uniform grid spacing $\Delta x/c = 0.02$. During the simulation, surface pressure p_s relative to the ambient pressure p_∞ is recorded at 11 predefined sensor locations (see figure 2). The pressure coefficient is computed using the standard definition:

$$C_p = \frac{2(p_s - p_\infty)}{\rho U_\infty^2}. \quad (3)$$

For training purposes, the vorticity data are extracted from a tighter region within the computational domain: $(-1.5c, 3.3c) \times (-1.2c, 1.2c)$ in the x and y directions, respectively. This subdomain is selected to maintain a balance between computational efficiency and physical fidelity, ensuring the full evolution of the gust disturbance and its interaction with the airfoil and wake are accurately captured. At each AoA, one undisturbed (baseline) case and 60 randomized gust cases are simulated, resulting in a dataset comprising 5 undisturbed cases and 300 disturbed (each with a single gust passage) cases in total. Each case is computed over 10 nondimensional convective time units, defined as $t = t'U_\infty/c$, where t' is the dimensional time. This time horizon ensures that at least two full vortex shedding cycles are captured. Flow fields are sampled at a uniform time interval of $\Delta t = 0.02$, yielding 500 snapshots per case. Altogether, the dataset consists of 152500 flow snapshots (vorticity field, surface pressure at the designated sensor locations, and lift force) spanning a wide range of aerodynamic conditions. The flow system states are defined as the vorticity field and the corresponding lift coefficient, which are to be estimated by assimilating synthetic surface pressure measurements.

2.2 Finding the low-dimensional latent space

To enable efficient data assimilation and accurate flow reconstruction, we first construct a compact, low-dimensional representation of the high-dimensional flow state. This reduced-order space is designed to capture the dominant coherent structures in the vorticity field, along with the associated lift dynamics, and serves as the latent state space for sequential filtering. To achieve this, we extend the concept of the lift-augmented autoencoder introduced by Fukami and Taira (2023) and adapt it to the requirements of our framework. The architecture of the resulting nonlinear physics-augmented autoencoder is illustrated in Figure 3 and table 1. In this model, the high-dimensional vorticity field $\boldsymbol{\omega} \in \mathbb{R}^l$ is encoded into a low-dimensional latent vector $\boldsymbol{\xi} \in \mathbb{R}^n$ via a neural network encoder \mathcal{F}_e . The latent representation $\boldsymbol{\xi}$, with $n \ll (l + 1)$, is then passed through a decoder \mathcal{F}_d to reconstruct not only the original vorticity field but also the corresponding lift coefficient and surface pressure values at prescribed sensor locations. This design ensures that the latent space retains sufficient information relevant to both global flow structure and aerodynamic observables.

The network parameters \mathbf{W} —comprising all weights and biases—are optimized by minimizing the following composite loss function with weight coefficients β :

$$\begin{aligned} \mathbf{W} = \arg \min_{\mathbf{W}} (\mathcal{L}_{AE}) = \arg \min_{\mathbf{W}} & \left(\underbrace{\beta_{\boldsymbol{\omega}} \|\boldsymbol{\omega} - \hat{\boldsymbol{\omega}}\|_2^2}_{\text{vorticity reconstruction}} + \underbrace{\beta_{\mathbf{p}} \|\mathbf{p} - \hat{\mathbf{p}}\|_2^2}_{\text{pressure reconstruction}} \right. \\ & \left. + \underbrace{\beta_{C_L} \|C_L - \hat{C}_L\|_2^2}_{\text{lift reconstruction}} + \underbrace{\beta_t \|\boldsymbol{\xi}_{t+1} - 2\boldsymbol{\xi}_t + \boldsymbol{\xi}_{t-1}\|_2^2}_{\text{temporal smoothness}} \right). \end{aligned} \quad (4)$$

Here, the lift and pressure reconstruction terms are incorporated into the loss function \mathcal{L}_{AE} to regularize the learned latent space and ensure that it remains informative with respect to key aerodynamic quantities. Notably, this formulation learns the observation operator—mapping the low-dimensional latent states $\boldsymbol{\xi}$ to surface pressure coefficient measurements, $\mathbf{p} = \mathbf{h}_{\mathbf{W}}(\boldsymbol{\xi}) \in \mathbb{R}^d$ —during the training process. Rather than training a separate network to learn the observation mapping post hoc, we integrate it directly into the autoencoder training. This joint learning approach has two key advantages: (1) it constrains the latent space to remain consistent with the pressure signatures, thus promoting sensor-relevant representations; and (2) it improves the accuracy and robustness of the learned observation operator while accelerating convergence during training. By embedding observability constraints (though partial) within the compression task, the resulting latent space not only captures the dominant flow structures but also preserves essential information required for downstream tasks such as state estimation and control. As a result, the decoder reconstructs vorticity field and lift as the original flow states, as well as pressure observations.

Conventional autoencoders process each data snapshot independently, disregarding the temporal correlations inherent in a transient fluid flow. This neglect often results in suboptimal compression, jagged or non-smooth latent trajectories, and poor generalization when extrapolating over time. However, for systems governed by smoothly evolving physical processes, such as transient fluid flow, the reduced latent space should ideally preserve this temporal quality. In other words, smooth evolution in the original state space should be mirrored by equally smooth trajectories in the latent representation to ensure physically meaningful and dynamically consistent encoding. To address this issue, we introduce a temporal regularization term that penalizes abrupt changes in the latent space from one input snapshot to the next in the sequence. Specifically, we enforce smoothness by minimizing the second time derivative of the latent variables. Compared to using a first derivative, this higher-order constraint has been shown to yield more stable and consistent representations during training (Xie et al. 2024). By discouraging sudden accelerations in the latent dynamics, this approach promotes smoother temporal evolution and mitigates spurious jumps, which is particularly important for sequential filtering and forecasting tasks.

The loss weights β_i in Eq. (4), where $i \in \{\boldsymbol{\omega}, \mathbf{p}, C_L, t\}$, are used to balance the relative contributions of each loss component to the total objective. These weights are carefully tuned to emphasize accurate reconstruction of the vorticity field and surface pressure—both of which are critical for ensuring reliable state estimation via the observation operator—while keeping the lift and temporal smoothness terms at comparable but lower magnitudes. Specifically, the lift and temporal losses are scaled to be approximately one order of magnitude smaller than the dominant reconstruction losses to serve as regularizers without overpowering the main signal. Based on empirical testing, we set $\beta_{\boldsymbol{\omega}} = 1.0$, $\beta_{\mathbf{p}} = 100.0$, $\beta_{C_L} = 1.0$, and $\beta_t = 5000.0$. For training, 70% of the total random gust cases—each spanning the full gust–airfoil interaction duration—are used for model optimization, while the remaining 30% are held out for validation and testing. Separating training and test sets by distinct gust encounters—rather

Table 1: Network architecture of the encoder, decoder, lift reconstruction, and pressure observation models. The activation function used is Tangent Hyperbolic.

Encoder		Decoder		Lift/Pressure Observation	
Layer	Data Size	Layer	Data Size	Layer	Data Size
Input	(240, 120, 1)	Dense	(128)	Dense	(32)
Conv2D (3,3,32)	(240, 120, 32)	Dense	(256)	Dense	(64)
Conv2D (3,3,32)	(240, 120, 32)	Dense	(288)	Dense	(32)
MaxPooling2D (2,2)	(120, 60, 32)	Reshape	(12, 6, 4)	Output 2 (Pressure)	(11)
Conv2D (3,3,16)	(120, 60, 16)	Conv2D (3,3,4)	(12, 6, 4)	Output 3 (Lift)	(1)
Conv2D (3,3,16)	(120, 60, 16)	Conv2D (3,3,4)	(12, 6, 4)		
MaxPooling2D (2,2)	(60, 30, 16)	UpSampling2D (5,5)	(60, 30, 4)		
Conv2D (3,3,8)	(60, 30, 8)	Conv2D (3,3,8)	(60, 30, 8)		
Conv2D (3,3,8)	(60, 30, 8)	Conv2D (3,3,8)	(60, 30, 8)		
MaxPooling2D (5,5)	(12, 6, 8)	UpSampling2D (2,2)	(120, 60, 8)		
Conv2D (3,3,4)	(12, 6, 4)	Conv2D (3,3,16)	(120, 60, 16)		
Conv2D (3,3,4)	(12, 6, 4)	Conv2D (3,3,16)	(120, 60, 16)		
Reshape	(288)	UpSampling2D (2,2)	(240, 120, 16)		
Dense	(256)	Conv2D (3,3,32)	(240, 120, 32)		
Dense	(128)	Conv2D (3,3,32)	(240, 120, 32)		
Dense (Latent vector)	(7)	Output 1 (Vorticity)	(240, 120, 1)		

than by randomly selecting individual snapshots across all cases—better reflects realistic deployment scenarios. In practice, models are trained on a subset of gust conditions and are expected to generalize to entirely new gust patterns, rather than merely interpolating between seen snapshots from the same cases. Training is terminated when the validation loss converges and plateaus (around epoch ≈ 2000), indicating stable learning.

2.3 Sequential filtering

Sequential filtering offers a principled framework for estimating the evolving state probability distribution of a dynamical system by continuously incorporating observational data as it becomes available. This study enables online inference of latent aerodynamic states from sparse and noisy surface pressure measurements, facilitated by learned forecast and observation models discussed in Section 2.4. For a comprehensive overview of sequential filtering methods—including their foundations and applications in aerodynamic contexts—we refer the reader to the recent review by Eldredge and Mousavi (2025).

Each sequential filtering algorithm step consists of two key substeps: the *forecast* (or prediction) step and the *analysis* (or update) step. In the forecast step, the system states—here, the latent variables $\boldsymbol{\xi}$ —are advanced in time using a dynamical model \mathbf{f} . When the governing dynamics are not known a priori, they can be learned from data using a NN, resulting in a learned forecast model \mathbf{f}_W , parameterized by network weights \mathbf{W} . The formulation assumes that the current state depends only on the immediate past state, thus preserving the Markov property of the underlying system dynamics within the reduced latent space. The forecast step provides an estimate of the prior distribution of states at that instant, $\pi(\boldsymbol{\xi}_k | \mathbf{p}_{1:k-1})$. Upon the arrival of new measurements, \mathbf{p}_k , the analysis step updates the prior to the posterior distribution, $\pi(\boldsymbol{\xi}_k | \mathbf{p}_{1:k})$. This Bayesian inference problem requires an observation operator \mathbf{h} that maps the latent state $\boldsymbol{\xi}$ to observables (e.g., surface pressures), with additive observation noise $\boldsymbol{\eta}$. As with the forecast model, this observation operator can be learned from data using a NN, \mathbf{h}_W , parameterized by its own set of weights.

In the classical setting, when both process and measurement noises are Gaussian and the forecast and observation operators are linear, the posterior distribution of the system states at each time step remains Gaussian and can be computed analytically. However, in fluid dynamic applications such as the one considered in this study, the forecast and observation operators are highly nonlinear, especially when learned via NNs. As a result, the posterior distribution becomes non-Gaussian, even if the noise distributions remain Gaussian. To address this, various extensions of the standard Kalman filter have been developed for nonlinear systems. Among them, the ensemble Kalman filter (EnKF) has proven particularly effective, especially in high-dimensional state spaces. Originally introduced by Evensen (1994), the EnKF approximates the distribution of system states using a finite ensemble of samples. It has been successfully applied to a wide range of problems, including in fluid dynamics and reduced-order modeling (da Silva and Colonius 2018, Moldovan et al. 2021, Le Provost and Eldredge 2021, Eldredge and Mousavi 2025).

In the EnKF framework, an ensemble of latent states $\{\boldsymbol{\xi}^i\}_{i=1}^M$ is drawn from some initial prior distribution. During the forecast step, each ensemble member is independently propagated forward in time using the learned dynamics model:

$$\boldsymbol{\xi}_{k|k-1}^i = \mathbf{f}_W(\boldsymbol{\xi}_{k-1}^i) + \mathbf{w}_k^i, \quad (5)$$

where $\mathbf{w} \sim \mathcal{N}(0, \mathbf{Q})$ represents the process noise and \mathbf{Q} is an empirical covariance, determined from the residual differences between predicted and true latent trajectories over all test cases. This approach is designed to balance the tradeoff between bias and variance in the ensemble of states.

The observation operator is then used to calculate the predicted observation associated with each ensemble member:

$$\mathbf{p}_k^i = \mathbf{h}_W(\boldsymbol{\xi}_{k|k-1}^i) + \boldsymbol{\eta}_k^i, \quad (6)$$

where $\boldsymbol{\eta}$ denotes the observation noise, modeled as independent and identically (Gaussian) distributed (i.i.d.) random variables with covariance $\boldsymbol{\Sigma}_p$. In this context, its standard deviation (square root of diagonal elements in $\boldsymbol{\Sigma}_p$) is fixed for all sensors and set equal to the mean observation error computed from the learned observation operator on the test aerodynamic cases (except in some experiments in which the noise of selected sensors is increased to simulate sensor failure). Similar to the process noise, this approach attempts to balance bias and variance in the measurement ensemble.

When a new observation becomes available, each ensemble member is updated during the analysis

step using the Kalman update formula:

$$\boldsymbol{\xi}_k^i = \boldsymbol{\xi}_{k|k-1}^i + \mathbf{K}_k \left(\mathbf{p}_k^* - \mathbf{h}_W(\boldsymbol{\xi}_{k|k-1}^i) - \boldsymbol{\eta}_k^i \right), \quad (7)$$

where \mathbf{p}_k^* denotes the true observation, and the term in parentheses is referred to as the *innovation*—the discrepancy between the actual and predicted observations. The Kalman gain \mathbf{K}_k determines how much weight is given to the new observation relative to the predicted state and is computed as $\mathbf{K} = \boldsymbol{\Sigma}_{\boldsymbol{\xi}\mathbf{p}} \boldsymbol{\Sigma}_{\mathbf{p}}^{-1}$, where $\boldsymbol{\Sigma}_{\boldsymbol{\xi}\mathbf{p}}$ is the cross-covariance between the state and observation ensembles; it is approximated empirically from the ensemble. This update strategy enables EnKF to provide efficient and robust posterior estimation, even in complex, nonlinear, and partially observed systems.

Although the EnKF operates in a low-dimensional latent space, spurious correlations between latent states and observations can still arise, particularly when latent variables encode global flow features or when the system involves elliptic couplings such as the pressure Poisson equation. These correlations may introduce non-physical corrections in directions that are weakly constrained by the sensors. To mitigate this, we adopt the low-rank Ensemble Kalman Filter (LREnKF) of Le Provost et al. (2022), which restricts the update to the dominant eigenmodes of the state-observation cross-covariance. This projection acts as an implicit localization, filtering out poorly observed directions and yielding more efficient, stable updates. The method has been demonstrated successfully in point-vortex estimation problems (Le Provost et al. 2022, Eldredge and Mousavi 2025) and is well-suited to our setting with limited sensor coverage and complex latent structure.

The LREnKF effectively rotates the state and observation spaces into lower-dimensional subspaces spanned by the most informative directions in each space, and performs the state update in these subspaces. Following Cui and Zahm (2021), in a nonlinear Gaussian setting, the most informative correction directions in the state space can be identified via the state space Gramian, defined as:

$$\mathbf{C}_{\boldsymbol{\xi}} = \int \left(\boldsymbol{\Sigma}_{\mathbf{p}}^{-1/2} \nabla \mathbf{h}_W(\boldsymbol{\xi}) \boldsymbol{\Sigma}_{\boldsymbol{\xi}}^{1/2} \right)^T \left(\boldsymbol{\Sigma}_{\mathbf{p}}^{-1/2} \nabla \mathbf{h}_W(\boldsymbol{\xi}) \boldsymbol{\Sigma}_{\boldsymbol{\xi}}^{1/2} \right) d\pi(\boldsymbol{\xi}) \in \mathbb{R}^{n \times n}, \quad (8)$$

where the expectation is taken with respect to the prior distribution. Here, $\nabla \mathbf{h}_W(\boldsymbol{\xi})$ denotes the Jacobian of the observation operator, computed via automatic differentiation within the NN framework, and $\boldsymbol{\Sigma}_{\boldsymbol{\xi}}$ is the prior state covariance matrix. By construction, $\mathbf{C}_{\boldsymbol{\xi}}$ is positive semi-definite, and its eigendecomposition $\mathbf{C}_{\boldsymbol{\xi}} = \mathbf{V} \boldsymbol{\Lambda}_{\boldsymbol{\xi}}^2 \mathbf{V}^T$ yields an orthonormal basis $\mathbf{V} \in \mathbb{R}^{n \times n}$ for the state space, with corresponding eigenvalues $\boldsymbol{\Lambda}_{\boldsymbol{\xi}} \in \mathbb{R}^{n \times n}$. In a similar manner, the observation space Gramian $\mathbf{C}_{\mathbf{p}}$ was defined by Le Provost et al. (2022) as

$$\mathbf{C}_{\mathbf{p}} = \int \left(\boldsymbol{\Sigma}_{\mathbf{p}}^{-1/2} \nabla \mathbf{h}_W(\boldsymbol{\xi}) \boldsymbol{\Sigma}_{\boldsymbol{\xi}}^{1/2} \right) \left(\boldsymbol{\Sigma}_{\mathbf{p}}^{-1/2} \nabla \mathbf{h}_W(\boldsymbol{\xi}) \boldsymbol{\Sigma}_{\boldsymbol{\xi}}^{1/2} \right)^T d\pi(\boldsymbol{\xi}) \in \mathbb{R}^{d \times d}. \quad (9)$$

Like its state space counterpart, $\mathbf{C}_{\mathbf{p}}$ is positive semi-definite, and its eigendecomposition $\mathbf{C}_{\mathbf{p}} = \mathbf{U} \boldsymbol{\Lambda}_{\mathbf{p}}^2 \mathbf{U}^T$ yields an orthonormal basis $\mathbf{U} \in \mathbb{R}^{d \times d}$ for the observation space, with corresponding eigenvalues $\boldsymbol{\Lambda}_{\mathbf{p}} \in \mathbb{R}^{d \times d}$. Both Gramians can be efficiently approximated via the Monte Carlo method over the prior ensemble. In practice, the eigenvalues are sorted in descending order, and only the leading $r_{\boldsymbol{\xi}} \leq n$ eigenmodes of the state space Gramian and the leading $r_{\mathbf{p}} \leq d$ eigenmodes of the observation space Gramian are retained for assimilation. These ranks are typically chosen to capture a prescribed fraction $\in [0, 1]$ of the cumulative normalized energy in the corresponding eigenvalue spectra.

The Kalman update can then be performed efficiently within this informative subspace by projecting the prior states onto the dominant eigenvectors \mathbf{V} in the state space and projecting the innovation onto the dominant eigenvectors \mathbf{U} in the observation space. After correction in this reduced subspace, the updated states are lifted back into the original latent space at each assimilation step. Accordingly, the Kalman update formula in Eq. (7) can be factorized in the LREnKF framework as:

$$\boldsymbol{\xi}_k^i = \boldsymbol{\xi}_{k|k-1}^i + \boldsymbol{\Sigma}_{\boldsymbol{\xi}}^{1/2} \mathbf{V} \check{\mathbf{K}}_k \mathbf{U}^T \boldsymbol{\Sigma}_{\mathbf{p}}^{-1/2} \left(\mathbf{p}_k^* - \mathbf{h}_W(\boldsymbol{\xi}_{k|k-1}^i) - \boldsymbol{\eta}_k^i \right), \quad (10)$$

where the reduced Kalman gain is computed in the low-dimensional informative subspace as $\check{\mathbf{K}} = \boldsymbol{\Sigma}_{\check{\boldsymbol{\xi}}\check{\mathbf{p}}} \boldsymbol{\Sigma}_{\check{\mathbf{p}}}^{-1} \in \mathbb{R}^{r_{\boldsymbol{\xi}} \times r_{\mathbf{p}}}$. Here, $\boldsymbol{\Sigma}_{\check{\boldsymbol{\xi}}\check{\mathbf{p}}}$ and $\boldsymbol{\Sigma}_{\check{\mathbf{p}}}$ denote the state-observation cross-covariance and observation covariance, respectively, computed from the projected ensemble members. During each state correction, the innovation for ensemble member i is first computed from the terms inside the parentheses, representing the difference between the measured and predicted pressures at the sensor locations. This innovation is then whitened by multiplying by the inverse square root of the observation error covariance, $\boldsymbol{\Sigma}_{\mathbf{p}}^{-1/2}$, to

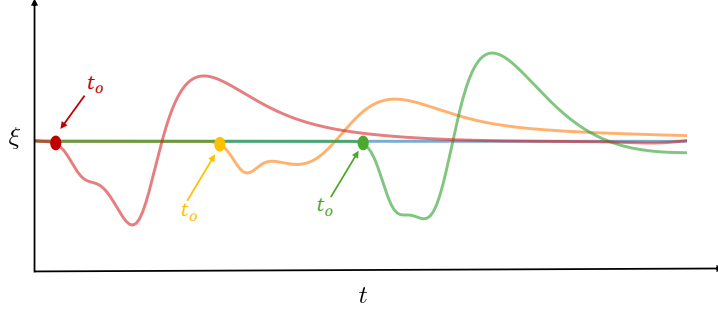


Figure 4: Bifurcation in learned latent trajectories for various gust-encounter aerodynamic cases, with each trajectory shown in a different color. For each case, the latent trajectory deviates from its corresponding undisturbed path (base flow with the airfoil at $\alpha = 20^\circ$) at the gust onset time t_o , reflecting the system’s response to external disturbance.

normalize the observation noise to unit variance. The whitened innovation is subsequently projected onto a reduced-dimensional observation subspace spanned by the dominant observation modes, \mathbf{U} . Within this subspace, the reduced Kalman gain, $\tilde{\mathbf{K}}_k$, maps the informative observation directions to the corresponding directions in the state subspace. The resulting update is then lifted back to the full state space using the dominant state modes, \mathbf{V} , and scaled (de-whitened) by the square root of the state covariance, $\Sigma_\xi^{1/2}$. A detailed description of the LREnKF algorithm is provided in Le Provost et al. (2021). This formulation ensures that the assimilation update only acts along directions that are both dynamically significant and well-informed by the available measurements, thereby improving robustness and reducing the impact of spurious correlations.

2.4 Learning surrogate models in the latent space

As described in Section 2.3, the two essential components for the sequential filter are the forecast and observation operators. We have already learned a surrogate observation operator, $\mathbf{p} = \mathbf{h}_\mathbf{W}(\xi)$, by virtue of the side network in our physics-augmented autoencoder architecture. With the low-dimensional latent states ξ established via the autoencoder, we now aim to learn the surrogate model that governs the temporal evolution of the flow state in this reduced latent space. These surrogate models replace traditional high-fidelity solvers by approximating the forecast and observation operators directly in the reduced space, enabling fast and efficient DA. For a comprehensive overview of various approaches to learning surrogate models for dynamical systems, readers are referred to Bach et al. (2024).

Sequential DA requires a transition model that governs the temporal evolution of the system states. As discussed in Section 1, filtering methods such as the Kalman filter are derived under the assumption of Markovian dynamics, where the future state depends solely on the current state. To model latent dynamics in a Markovian fashion, we employ a Neural ODE framework that learns a continuous-time dynamical system in the latent space, expressed as:

$$\frac{d\xi}{dt} = \tilde{\mathbf{f}}_\mathbf{W}(\xi), \quad (11)$$

where $\tilde{\mathbf{f}}_\mathbf{W}$ is a NN parametrized by \mathbf{W} . This approach offers several advantages over traditional discrete-time models: it allows for variable time intervals, supports evaluation at arbitrary time points, and enables adaptive time integration strategies. To recover a standard discrete-time state transition model required by filtering, we discretize Eq. (11) using a first-order forward Euler scheme:

$$\xi_k = \mathbf{f}_\mathbf{W}(\xi_{k-1}), \quad (12)$$

where $\mathbf{f}_\mathbf{W}(\xi_{k-1}) = \tilde{\mathbf{f}}_\mathbf{W}(\xi_{k-1}) \Delta t + \xi_{k-1}$ with k the time index.

A schematic illustration of latent trajectories under different random gust conditions is shown in Figure 4. Prior to the introduction of the gust, all trajectories closely follow the undisturbed path, indicating that the system initially behaves as in the baseline case. For simplicity in the illustration in Figure 4, the baseline is flat, corresponding to a steady flow with a time-invariant point in the latent space. However, most cases considered in this work will have time-periodic baseline trajectories reflecting the bluff-body vortex shedding of a wing at a significant angle of attack. When the gust

is introduced at a randomly selected time (denoted by solid circles in the figure) within the shedding cycle, the corresponding trajectory deviates from the baseline and subsequently returns to the baseline path once the gust has convected sufficiently far from the airfoil. This bifurcation behavior captures the transient influence of the gust on the flow dynamics. The purpose of the forecast model is not to predict the point of bifurcation from the baseline (a task that is assigned to the filter’s measurement update), but rather, to capture the subsequent dynamics of the flow in the latent space. To ensure the Neural ODE accurately models these dynamics and to provide diverse initial conditions across different aerodynamic cases, snapshots for each disturbed case are restricted to begin 10 time steps (Δt) after the gust onset and continue for 200 snapshots, encompassing the full gust–airfoil interaction. This targeted training strategy enables the Neural ODE to learn the disturbed dynamics effectively, ensuring that during sequential filtering, it can faithfully track the perturbed latent trajectories shortly after the measurement-corrected state aligns with the true disturbed path. The network architecture is listed in Table 2 and is trained on both undisturbed and disturbed cases.

Table 2: Network architecture of the Neural ODE. The activation function used is Tangent Hyperbolic.

Neural ODE	
Layer	Data Size
Input	(240, 120, 1)
Dense	(128)
Dense	(256)
Dense	(128)
Dense (Latent Vector)	(7)

In most applications, Neural ODEs are trained by minimizing a one-step prediction error. However, this approach has a well-known limitation: the forward model is trained using teacher forcing on one-step losses, so during inference, when the model is rolled out autoregressively, prediction errors accumulate over time, leading to degradation in accuracy. To mitigate this issue, we also include a loss term that penalizes prediction error over a long-time prediction horizon. Specifically, the model parameters \mathbf{W}_f are obtained by solving:

$$\mathbf{W}_f = \arg \min_{\mathbf{W}_f} \left(\underbrace{\beta_{f,1} \|\boldsymbol{\xi}_t - \hat{\boldsymbol{\xi}}_t\|_2^2}_{\text{rollout loss}} + \underbrace{\beta_{f,2} \|\boldsymbol{\xi}_{t+1} - (f(\boldsymbol{\xi}_t) + \boldsymbol{\xi}_t)\|_2^2}_{\text{one-step loss}} \right), \quad (13)$$

where $\beta_{f,1}$ and $\beta_{f,2}$ are weighting factors assigned to the rollout and one-step losses, respectively. To emphasize accurate prediction during the initial phase of gust–airfoil interaction, we decay the rollout weighting over time as $\beta_{f,1} = 1 - 0.5(t - 1)/(T - 1)$ for $t = 1, \dots, T$, with T denoting the final rollout time step. This schedule ensures that higher weight is given to early predictions during disturbance events and gradually reduces the contribution of later predictions within the rollout horizon. In this formulation, we set $\beta_{f,2} = 150$, as it was observed that these weights give better predictions.

With the surrogate models now learned in the reduced-order space, all necessary components for sequential DA are in place.

3 Results and discussion

In this section, we first focus on the compression of full-dimensional flow data into a reduced-dimensional latent space via a physics-augmented autoencoder. Then, we discuss the training of surrogate models necessary for filtering. Finally, we present results for data assimilation in the latent space.

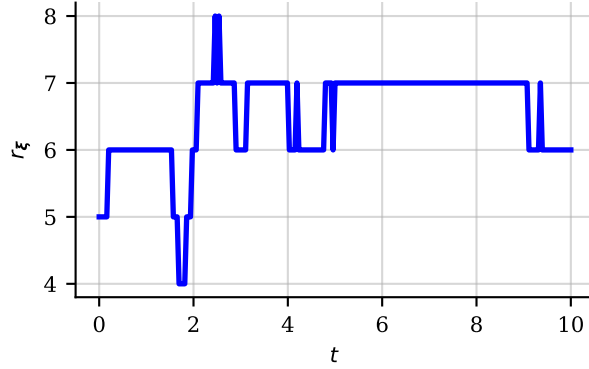


Figure 5: The history of state rank r_{ξ} for $n = 10$. The flow condition is $(\alpha = 60^\circ, D_y = -0.71, \sigma = 0.12, y_o = -0.19, t_o = 3.3)$.

3.1 Construction of latent space and learned operators

Previous researchers have demonstrated that high-dimensional disturbed aerodynamic flows can be effectively projected onto very low-dimensional manifolds, as low as three-dimensional, using nonlinear autoencoders (Fukami and Taira 2023, Mousavi and Eldredge 2025, Fukami et al. 2025). However, it is important to note that when additional regularization terms—such as temporal smoothness and pressure reconstruction losses—are incorporated into the training objective, the dimensionality of the latent space must generally be increased to compensate for the stricter constraints imposed on the encoded representation. This increase provides the necessary degrees of freedom to adequately capture the dominant flow features and enhance their observability within the compressed subspace.

To determine an appropriate latent-space dimension n , we take the following systematic approach, guided both by the error trends in training the autoencoder and the effective state rank of the sequential filtering in the LREnKF. We first conducted a systematic analysis using the network architecture shown in figure 3 and table 1. Specifically, we examined the validation loss as a function of latent dimension and observed that the loss plateaued beyond $n = 7$, indicating diminishing returns in reconstruction fidelity with further increases in dimensionality. This finding is corroborated by a complementary experiment in which the dataset was compressed into a 10-dimensional latent space, followed by sequential DA. As illustrated in figure 5, rarely did more than seven directions in the latent space exhibit sensitivity to variations in the sensor measurements, further supporting the choice of $n = 7$. While it is possible to adopt a higher-dimensional latent representation, the goal in this work is to encode the high-dimensional flow field into the most compact latent space that still preserves the information necessary for accurate state estimation. Conversely, selecting a latent dimension smaller than seven risks excessive compression, compromising the uniqueness and identifiability of the latent representation of flow trajectories required for robust sequential filtering and inference. Overall, the choice of latent dimension reflects a tradeoff among reconstruction accuracy, compactness of the representation, and degree of identifiability required for reliable sequential estimation. Based on these analyses, we set $n = 7$ as the latent dimension in this study.

To explore the extent to which the latent dynamics are interpretable, figure 6 presents the histories of the latent vector components for several independent disturbed cases at $\alpha = 40^\circ$. The undisturbed flow over the airfoil at a high AoA (such as the case in this figure represented by black curves) exhibits characteristic periodic behavior, which is also clearly reflected in the latent space representation. The time window shown spans slightly more than two full vortex shedding cycles. The bifurcation highlighted earlier in figure 4 is evident here as well, manifesting as divergence in the latent component histories due to the gust encounters at random phases of the shedding cycle. While these trajectories implicitly encode the influence of gust characteristics, vortex dynamics, and their interactions, the mapping between individual latent variables and specific physical phenomena remains difficult to disentangle. Determining which components of the latent vector correspond to particular aspects of the flow or external disturbances would require targeted analyses beyond the scope of this work. A systematic study aimed at interpreting these latent representations and rigorously connecting them to the underlying flow physics (e.g. Smith et al. (2024)) remains an important direction for future research.

It is worth emphasizing that the reconstruction of lift, pressure, and vorticity fields is achieved through the decoder part of the physics-augmented autoencoder. The performance of the decoder can be evaluated

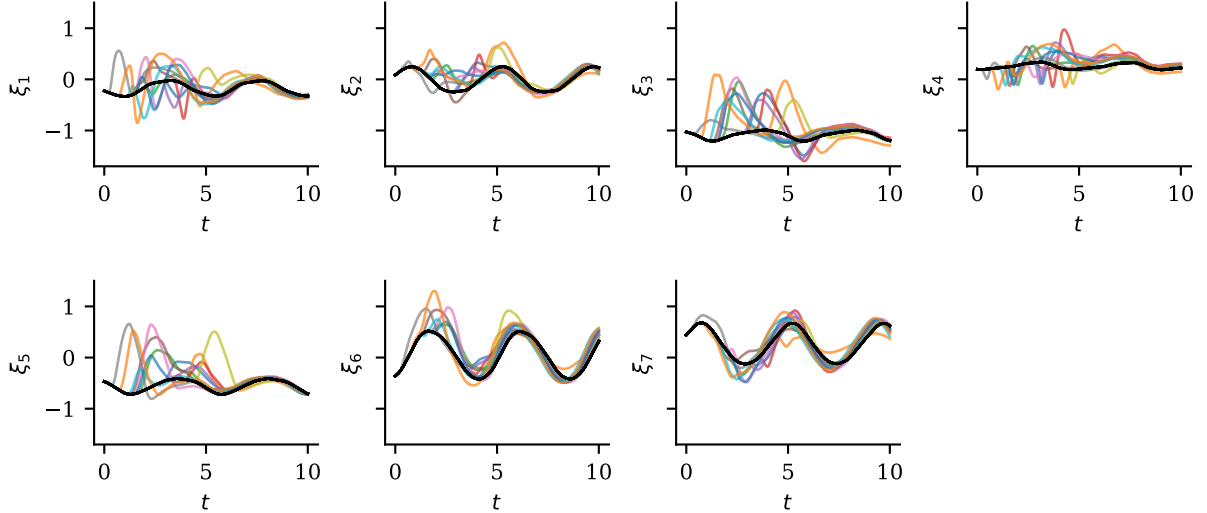


Figure 6: Latent trajectories for several disturbed aerodynamic cases. Each color corresponds to a different random gust introduced at a random time within the vortex shedding cycle, interacting with the airfoil at an AoA of $\alpha = 40^\circ$, while the black curves correspond to the undisturbed case.

by comparing the decoded fields against the reference input fields. Figure 7 illustrates the results for five test aerodynamic cases under different AoA, showing reconstructed vorticity, lift coefficient, and one sensor’s surface pressure coefficient for each case. As evident in this figure, the reconstruction of the lift and the pressure coefficients (i.e., the learned observation operator) exhibit excellent performance across all four test cases. It is also clear that the presence of a disturbance causes the lift and pressure signals to deviate from their undisturbed periodic trajectories, returning to these trajectories once the gust convects downstream from the airfoil. The stronger the disturbance, the greater is the deviation of the lift and surface pressure readings from the baseline periodic path. The performance of the vorticity decoder, quantified by the reconstruction error, $\varepsilon = \|\boldsymbol{\omega} - \hat{\boldsymbol{\omega}}\|_2 / \|\boldsymbol{\omega}\|_2$, is overall satisfactory, especially considering the compact latent representation used in this study. As expected, the reconstruction error increases when a disturbance is present in the domain. The average pressure observation error over the whole test cases is used to determine the standard deviation of the random observation noise $\boldsymbol{\eta}$ in Eq. (6). This is determined to be equal to 0.012 for the test set in this study.

Dipole gusts consist of a positive and a negative vorticity lobe convecting across the airfoil. Their aerodynamic impact can be understood in terms of their interaction with the primary vortical structures of the separated shear layer. In all investigated cases, a consistent aerodynamic pattern emerges in response to dipole gusts. As the positive lobe of the dipole interacts with the primary negative LE vortex, the effective angle of attack increases transiently, elevates circulation, which produces a sharp lift surge. Shortly thereafter, the negative lobe arrives and disrupts the vortex structure, leading to a rapid drop in lift.

Now that we have demonstrated successful state compression in tandem with an accurately learned observation operator, there remains one more verification step before proceeding to DA: assessing the performance of the learned forecast operator described in Section 2.4. Figure 8 illustrates the history of one predicted latent variable, ξ_2 , during gust passage in one of the test cases. Starting from the true initial state, the autoregressive prediction initially tracks the true trajectory but eventually diverges. At first glance, this deviation may seem unexpected, given that the model was explicitly trained with a rollout loss designed to prevent error accumulation over long prediction horizons. It is important to emphasize, however, that the one-step prediction remains highly accurate, as is essential for DA applications. Indeed, the learned forecast operator provides reliable short-term estimates during rollout predictions, ensuring that sequential updates in filtering can be based on precise time-local dynamics, even if longer-term rollout trajectories diverge. Despite the larger prediction error observed in this example, the inclusion of the rollout loss does stabilize the network: the error does not grow without bound over time. Rather, the discrepancy arises because, while the original high-dimensional dynamics are Markovian, this quality is not necessarily preserved when compressed into a low-dimensional latent space. In other words, two nearby initial conditions in the compressed representation can evolve into significantly different trajectories. This important limitation has been rigorously established in the

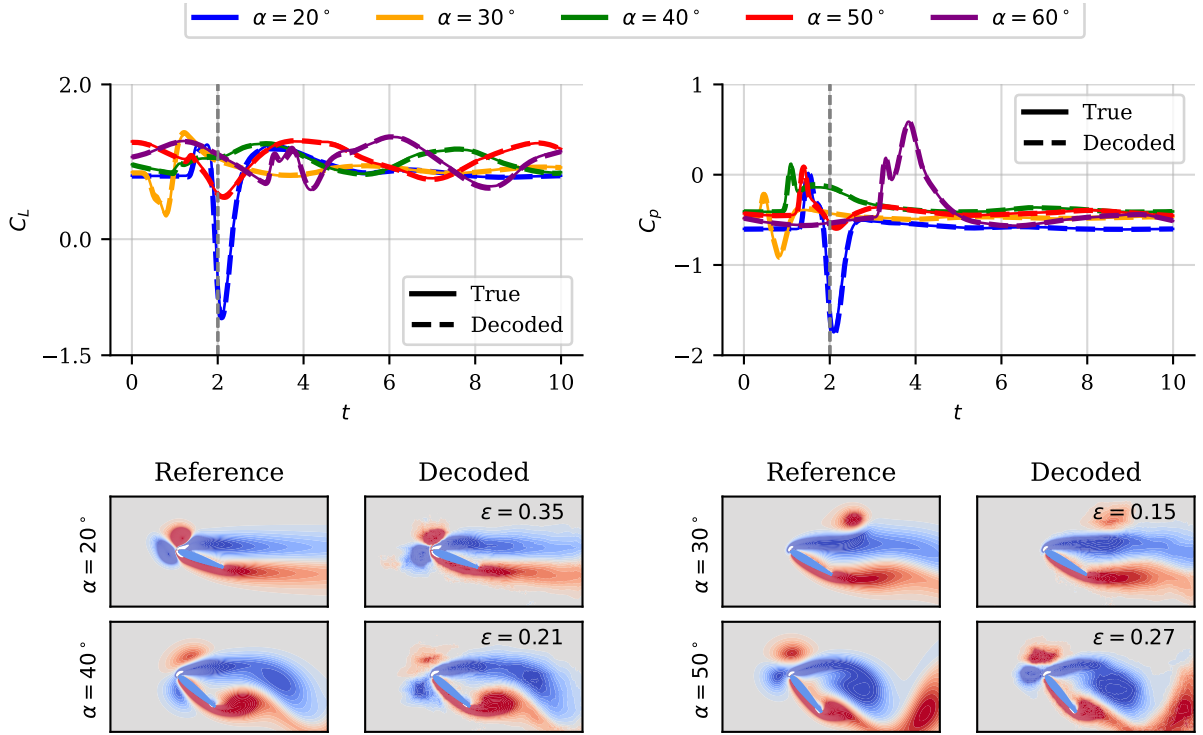


Figure 7: Comparison between the decoded and reference lift and pressure coefficients and vorticity fields for test cases under the following conditions: ($\alpha = 20^\circ$, $D_y = -1.9$, $\sigma = 0.1$, $y_o = 0.22$, $t_o = 1.5$); ($\alpha = 30^\circ$, $D_y = 0.44$, $\sigma = 0.08$, $y_o = 0.19$, $t_o = 0.5$); ($\alpha = 40^\circ$, $D_y = 0.24$, $\sigma = 0.19$, $y_o = -0.07$, $t_o = 1.1$); ($\alpha = 50^\circ$, $D_y = -0.64$, $\sigma = 0.2$, $y_o = 0.16$, $t_o = 1.4$). The pressure plot corresponds to sensor 7. All vorticity plots are shown at time $t = 2$, as indicated by the vertical dashed lines in the upper panel plots.

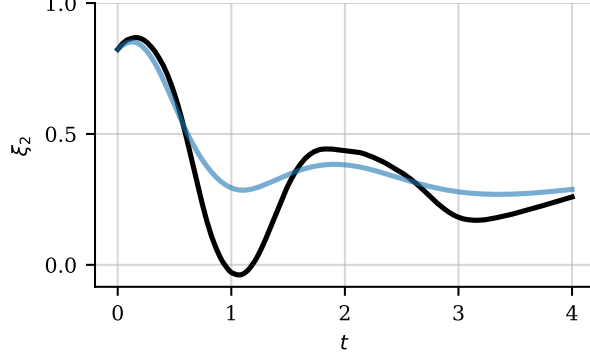


Figure 8: Example of the history of true (black) and predicted (blue, from the learned forecast operator) latent state for the airfoil at $\alpha = 20^\circ$ during a gust encounter.

foundational work of Zwanzig (1961) and Mori (1965). According to Mori–Zwanzig theory, the evolution of any reduced subspace can be decomposed into a Markovian term, a memory (history-dependent) term, and an unobservable (noise) term. As demonstrated by Ruiz et al. (2024), explicitly modeling the memory term can significantly improve predictive performance. Following this insight, one promising way to improve the forecast operator is to incorporate history dependence using memory-based NNs such as RNNs. However, this approach comes at the cost of breaking the Markovian assumption required by standard sequential filtering methods. Indeed, the philosophy of our current approach is that the responsibility for correcting deviations lies with the measurement update of each filter step. Thus, we deliberately choose to retain this imperfect, but short-term-accurate, forecast operator to evaluate the performance of our filtering framework under the realistic scenario of a non-ideal predictive model.

3.2 Sequential filtering examples

Now, everything is in place to set up the DA task. Pressure measurements from 11 sensors uniformly mounted on the airfoil (see figure 2) in CFD simulations with added noise are used for state estimation via the LREnKF framework. Each member of the ensemble of estimated latent states is then propagated through the pre-trained decoder of the network architecture shown in figure 3 to reconstruct both the lift coefficient and the vorticity field. For all cases in this section, a convergence study was performed, and we selected an ensemble size of $N_e = 200$. The ensemble members were initialized as Gaussian perturbations from the true state, always a latent representation of the undisturbed initial flow about the airfoil, with a variance of 10^{-4} . Each assimilation step is observed to take as fast as a few milliseconds.

The results are presented in figures 9 and 10 for the smallest and largest AoA considered in this study, namely $\alpha = 20^\circ$ and 60° , respectively. In these test cases, random disturbances are introduced at random instants within the first cycle. For both cases, the predicted lift coefficient shows excellent agreement with the true values throughout the assimilation horizon. The estimation closely tracks the temporal variations induced by gust disturbances, with uncertainty intervals remaining narrow except during the disturbance passage, when larger deviations naturally occur. This confirms that the assimilation effectively leverages the sparse pressure measurements to correct the latent state estimate in real time, even when the forecast operator alone exhibits significant predictive error.

In figures 9 and 10, the estimated ensemble statistics are compared against the decoded vorticity reconstructed from the true latent vectors, referred to as the *true decoded* vorticity. It is important to note that even the true decoded vorticity exhibits non-negligible reconstruction error relative to the reference field, which defines the attainable lower bound on prediction error. This field represents the best reconstruction achievable by the learned autoencoder. Accordingly, the prediction mean is evaluated relative to the true decoded field using the error metric $\varepsilon_d = \|\boldsymbol{\omega}_d - \hat{\boldsymbol{\omega}}\|_2 / \|\boldsymbol{\omega}_d\|_2$, where $\boldsymbol{\omega}_d$ denotes the true decoded vorticity. The vorticity reconstructions demonstrate similar trends: in all snapshots, the estimated ensemble mean fields are in good agreement with the true decoded vorticity, capturing the primary vortical structures and their evolution over time. As expected, reconstruction errors ε_d are largest immediately after the disturbance enters the domain and hits the tip of the airfoil, but progressively decrease as the estimator assimilates new observations and corrects the predicted state. However, the gust core as well as regions farther from the pressure sensors and near the periphery of the separated shear layers show larger deviations from the reference flow. This discrepancy can be

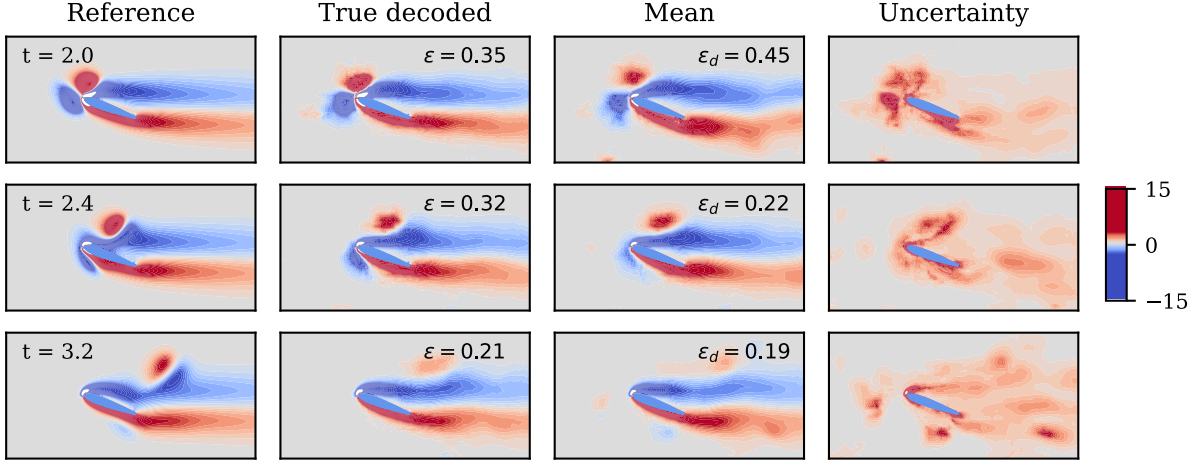
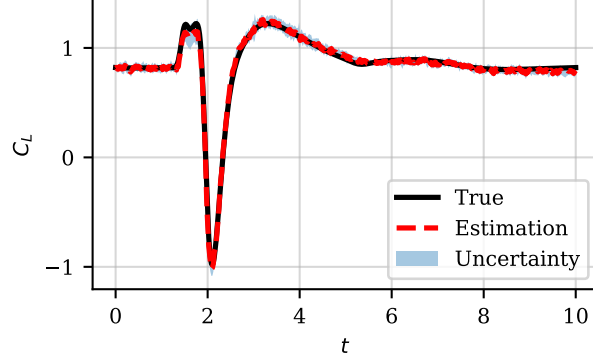


Figure 9: Estimated lift and vorticity field for disturbed aerodynamics at the condition ($\alpha = 20^\circ$, $D_y = -1.9$, $\sigma = 0.1$, $y_o = 0.22$, $t_o = 1.5$). The predicted ensemble mean along with the 95% confidence interval is shown for the lift coefficient and the vorticity field.

attributed to the lower sensitivity of the pressure sensors to flow variations in those areas, as reflected in the increased uncertainty of the estimates. Overall, the estimator remains highly confident and accurate in reconstructing the dominant flow features associated with both the disturbance and other large-scale vortical structures. Nonetheless, it is less certain about the precise strength of the gust and primary vortex boundaries, where the vortical structures are of a smaller scale and so contribute less to the surface pressure signatures.

To further elucidate the relationship between reconstruction error and the underlying observability properties of the estimator, we examine the temporal evolution of both the state rank r_ξ and observation rank r_p during the assimilation process. The state rank reflects the number of latent directions actively informed by observations and corrected by the measurement updates, whereas the observation rank quantifies the number of independent pressure observation modes that effectively inform the latent variables. The evolution of these ranks for a representative test case at the highest angle of attack, corresponding to figure 10, is shown in figure 11. The figure highlights the distinctly low-rank nature of the estimator: among the 11 available pressure sensors, the number of informative observation directions varies between 4 and 7 over time, while 5 to 7 latent directions are actively updated in the analysis step of the filter. This behavior was consistently observed across all angles of attack and random disturbance realizations. Notably, attempting DA with a full-rank EnKF in this context can lead to over- or under-correction of the state estimates due to spurious correlations and sampling noise, underscoring the necessity of rank truncation for robust and reliable flow reconstruction.

To better understand the structure of the latent variable updates, figure 12 presents the temporal evolution of four representative state modes— v_1 , v_2 , v_3 , and v_7 —at selected snapshots during the disturbance passage. These modes are the singular vectors of the state Gramian \mathbf{C}_ξ , sorted by descending singular values. Modes v_1 through v_3 , which correspond to well-observed directions, show relatively smooth and coherent spatial patterns and evolve consistently with the passage of the disturbance. In

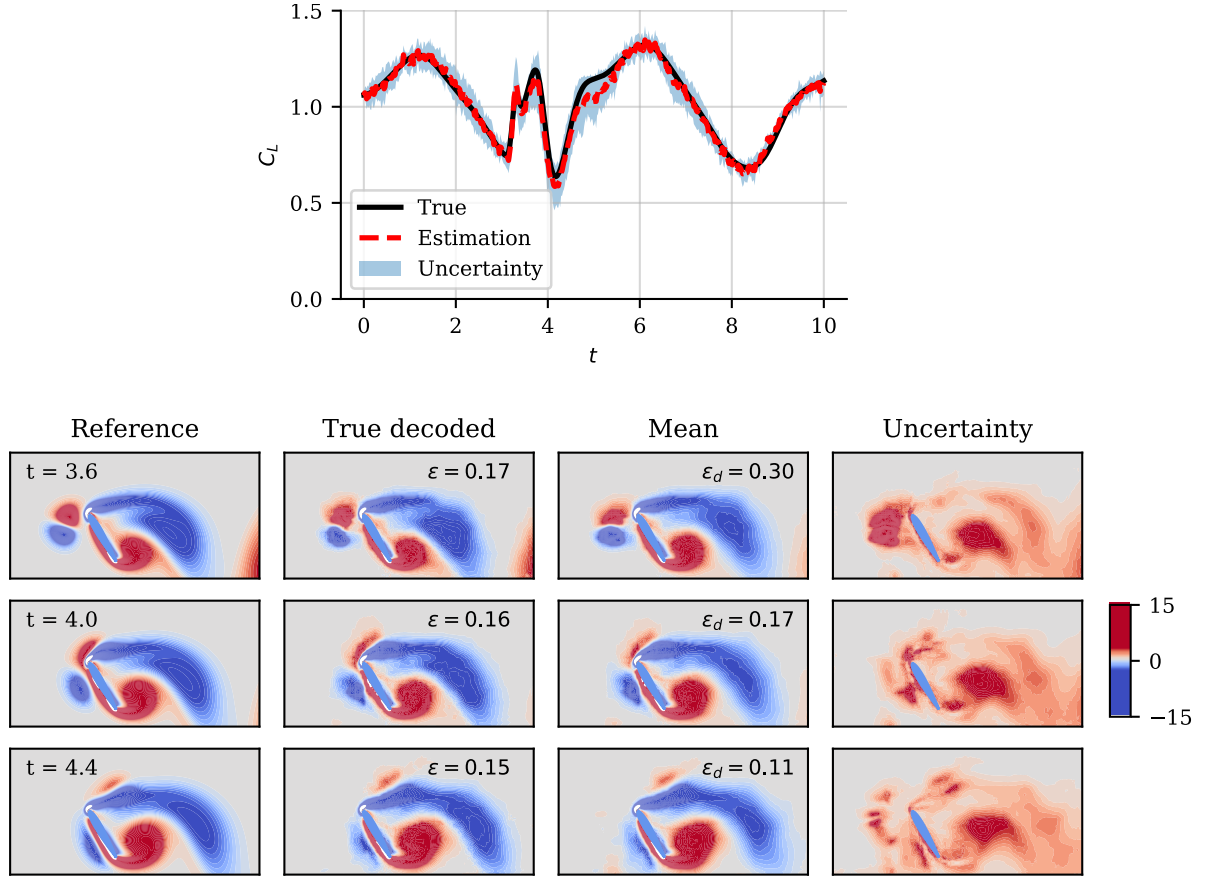


Figure 10: Estimated lift and vorticity field for disturbed aerodynamics at the condition ($\alpha = 60^\circ$, $D_y = -0.71$, $\sigma = 0.12$, $y_o = -0.19$, $t_o = 3.3$). The predicted ensemble mean along with the 95% confidence interval is shown for the lift coefficient and the vorticity field.

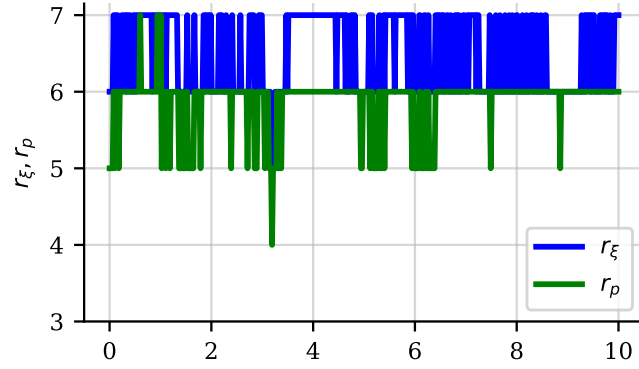


Figure 11: Effective state rank r_ξ and observation rank r_p for disturbed aerodynamics under the condition ($\alpha = 60^\circ$, $D_y = -0.71$, $\sigma = 0.12$, $y_o = -0.19$, $t_o = 3.3$).

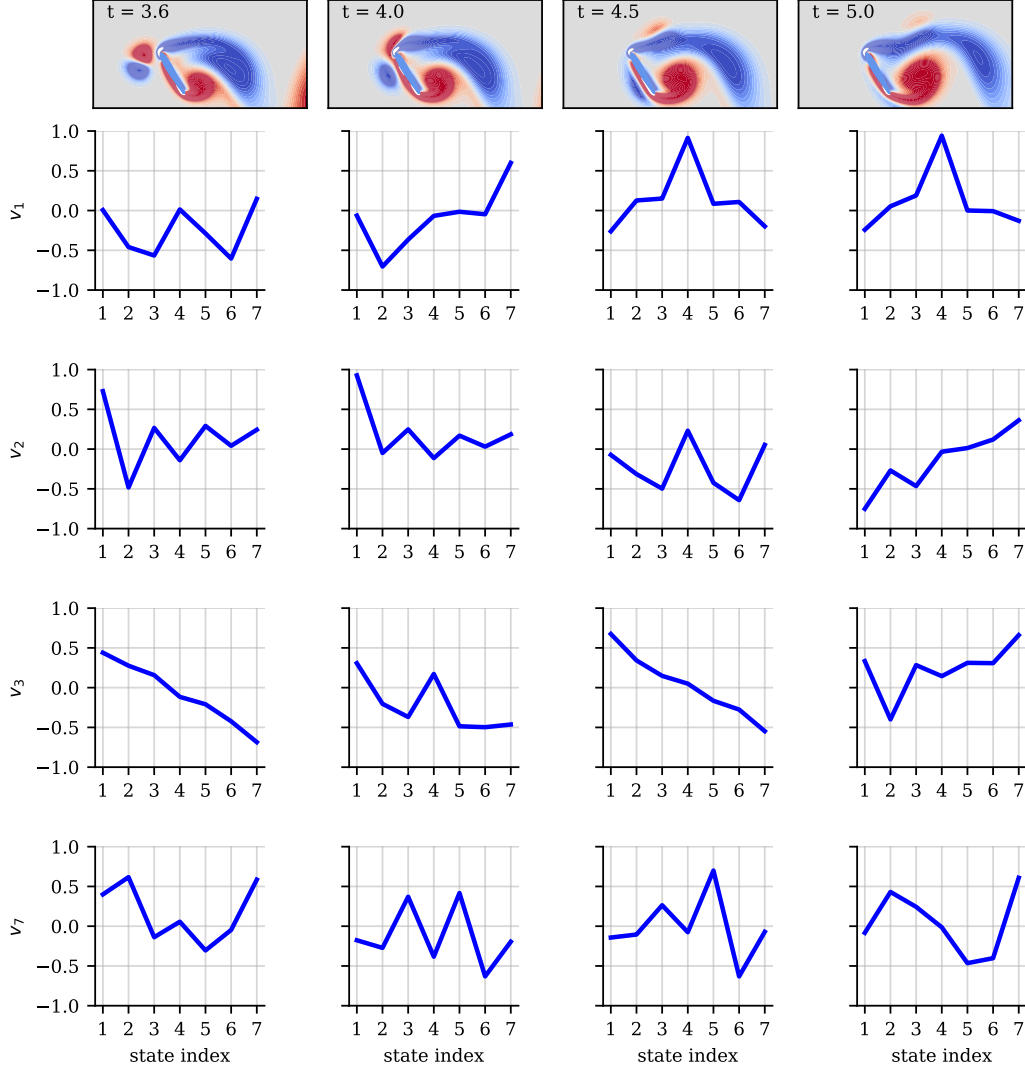


Figure 12: The first, second, third, and seventh latent state modes at four distinct time instances during the gust interaction for the case ($\alpha = 60^\circ$, $D_y = -0.71$, $\sigma = 0.12$, $y_o = -0.19$, $t_o = 3.3$).

contrast, mode v_7 , which lies closer to the nullspace of the Jacobian of the observation operator, exhibits noisier and less structured behavior, indicating that it is less informed by the pressure observations. These plots make clear that the weights in the state modes identify which latent directions are most strongly corrected during assimilation.

As observed in figure 12, the latent directions associated with very small eigenvalues correspond to modes that are effectively unobserved by the pressure sensors. For the case $\alpha = 20^\circ$, we conduct a dedicated investigation of these unobservable latent directions by explicitly constructing perturbations in the approximate nullspace of the Jacobian of the observation operator, $\nabla \mathbf{h}_{\mathbf{w}}$. The resulting vorticity reconstructions, shown in figure 13, illustrate that even substantial deviations in the latent state along these directions can produce predicted pressure measurements that remain well within the uncertainty bounds of the sensors, yet correspond to markedly different flow fields. This phenomenon provides a direct demonstration of the many-to-one mapping between latent representations and pressure signatures. Notably, the vorticity differences induced by nullspace perturbations manifest predominantly in regions where the sensors have limited sensitivity: the gust core, the separated shear layers along the suction side, and the wake. This explains the residual ambiguity and elevated uncertainty observed in the reconstructed flow fields in figures 9 and 10. The errors ε_d further highlight that unobservable latent

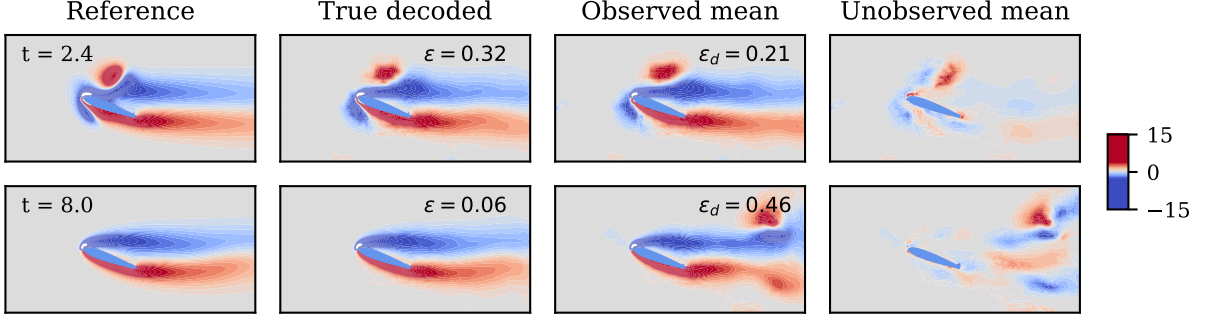


Figure 13: The unobservable vorticity plots for disturbed flow at condition ($\alpha = 20^\circ$, $D_y = -1.9$, $\sigma = 0.1$, $y_o = 0.22$, $t_o = 1.5$).

modes can contribute significantly to the overall vorticity prediction error. These results underscore that, in the absence of additional measurement modalities or prior regularization, multiple latent states can remain indistinguishable from the perspective of the available sensors, fundamentally limiting the estimator’s ability to uniquely resolve the true flow configuration. This ambiguity becomes more pronounced once the gust has moved away from the airfoil, a regime in which the pressure sensors exhibit reduced sensitivity to residual flow variations. As a result, the likelihood of multiple plausible latent solutions increases, particularly in regions or time intervals where the flow-induced pressure signals are weak. This issue could be mitigated by incorporating a maximum observability constraint during training the autoencoder detailed in section 2.2. We explored this strategy through a modified formulation that enforces a unique latent representation consistent with the pressure observations, leading to significantly improved accuracy in latent state estimation. However, under this constraint, the vorticity decoder exhibited heightened sensitivity to small perturbations in the latent variables, such that even minor estimation errors resulted in non-physical artifacts and substantial degradation in reconstruction quality. This tradeoff highlights the challenge of balancing observability in measurement space and robustness in high-dimensional state reconstruction when designing compressed latent-variable-based estimators for unsteady flow reconstruction.

It is also insightful to examine the observation modes corresponding to the sensor configuration and their role in informing state estimation. Figure 14 presents the leading and trailing observation eigenmodes—specifically u_1 , u_2 , u_3 , and u_{11} —with the same flow conditions as figure 12. The sensor indices follow the ordering shown in figure 3, where sensor 1 is located at the trailing edge on the upper surface, and the numbering proceeds counterclockwise around the airfoil, ending at the trailing edge on the lower surface. Each observation mode is a weighted combination of sensor outputs that, through the Kalman gain, most strongly influences the filter correction in a corresponding latent direction. For instance, u_1 reflects the most informative observation direction. The weight assigned to each sensor in these modes reflects its relative contribution to that direction in the observation space. From these plots, we observe that during the critical time interval $t \in [3.6, 4.0]$, when the gust approaches and begins interacting with the airfoil on the pressure side, leading-edge sensors 6 through 9 on the lower surface become the most responsive. These sensors exhibit consistently high contributions across the dominant observation modes, indicating their central role in informing the estimator throughout the gust-airfoil-wake interaction ($t \in [3.6, 5.0]$). While the relative contributions of other sensors vary over time, the leading-edge and lower-side sensors remain the most informative across modes and time steps.

It is worth emphasizing that this observation contrasts with findings from our earlier study (Mousavi and Eldredge 2025), in which the upstream disturbance was modeled using a Taylor vortex. A Taylor vortex typically introduces a stronger and more disruptive disturbance compared to a vortex dipole, leading to intense interaction with the primary shear layer and edge vortices on the suction side. As a result, the suction-side sensors were found to be highly sensitive and informative in that setting. In contrast, the dipole-like gust generated by Gaussian forcing in the present work interacts more locally with the pressure side, producing a more focused and asymmetric sensor response. This distinction highlights the importance of gust structure in shaping the spatial distribution of sensor informativeness and ultimately determining the directions along which the latent states can be effectively constrained.

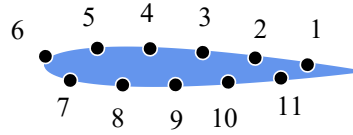
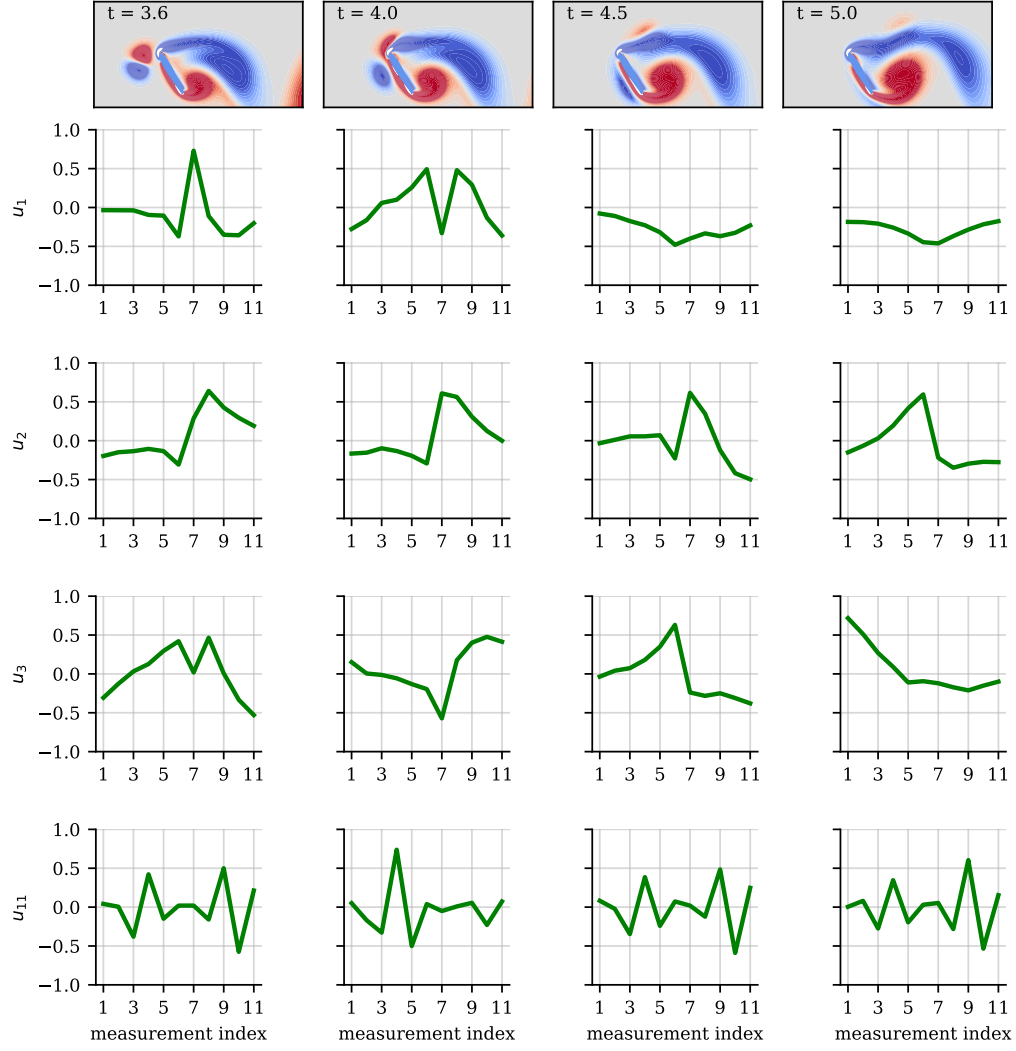


Figure 14: The first, second, third, and eleventh observation modes at four distinct time instances during the gust interaction for the case ($\alpha = 60^\circ$, $D_y = -0.71$, $\sigma = 0.12$, $y_o = -0.19$, $t_o = 3.3$). How the sensor numbers are ordered in the eigenvector plots is shown on the airfoil.

3.3 Sensor failure study

As shown in the preceding analysis, leading-edge sensors play a dominant role in informing the data assimilation process. A natural set of questions arises: What happens if a highly informative sensor fails or is removed? How significantly would this affect the accuracy of the state estimation? Would the estimator become unreliable simply due to the loss of a single, influential sensor? To address these questions, we investigate the effect of sensor dropout on flow estimation. A sensor can be effectively “dropped” by assigning it a much larger measurement noise variance, thereby diminishing its contribution in the assimilation update. Specifically, we simulate the failure of sensor 6, a leading-edge sensor identified as highly informative in figure 14, by increasing its variance by a factor of 100 relative to all other sensors. Data assimilation is then performed for the same flow condition presented in figure 14. For comparison, we also drop sensor 2, located near the trailing edge (TE) on the suction side—an area associated with minimal sensor response—in a separate setting and assess its impact relative to a baseline case where all sensors have equal uncertainty (see figures 10, 12, and 14).

The results shown in figure 15 reveal that dropping either sensor leads to only a modest increase in the average lift prediction error, indicating that the estimator remains robust in capturing global aerodynamic loads. However, the impact on the reconstructed vorticity field is more pronounced, particularly when sensor 6—located near the leading edge (LE) on the pressure side—is removed. In this case, more noticeable degradation is observed in regions near the gust core and the downstream wake. The corresponding posterior uncertainty fields reveal a clear increase in the variance of the vorticity estimates in those regions, indicating that sensor 6 plays a critical role in constraining the latent state components associated with the downstream evolution of the gust-induced flow structures. In contrast, dropping sensor 2—located near the TE on the suction side—has a negligible effect on both the reconstructed flow field and the associated uncertainty bounds. This suggests that sensor 2 contributes minimally to the information content of the observation operator in this particular flow regime and sensor configuration. On the other hand, the removal of sensor 6, which had a strong contribution to the leading observation modes (as seen in figure 14), significantly alters the structure of the dominant observation eigenvectors, evident in figure 16. Specifically, the eigenmodes reconfigure by suppressing the weight of sensor 6 to nearly zero and compensating by reallocating higher weights to its neighboring sensors (e.g., sensors 5, 7, and 8). This redistribution allows the estimator to partially recover the lost observability; however, the reconfigured observation space may not fully span the same latent directions as before. As a result, the effective observation rank may decrease, or the information associated with critical latent directions may be weakened. This potential degradation in observability leads to increased posterior uncertainty along certain state directions, particularly those associated with the spatial regions that sensor 6 was originally sensitive to. This explains the elevated uncertainty and local deterioration in vorticity reconstruction quality observed in the gust-impacted regions when sensor 6 is dropped.

To further assess the estimator’s robustness, we examine the scenario in which multiple sensors, here sensors 2, 6, and 11, fail simultaneously. The corresponding results are shown in figures 15 and 16. To recall, sensor 6 originally provided the most informative measurements, so the overall reconstruction quality is comparable to the case where only sensor 6 is removed, evident in the dominant observation modes illustrated in figure 16. Interestingly, the vorticity reconstruction is slightly improved in the three-sensor failure case, which may be attributed to sensors 2 and 11 being highly correlated with other active sensors. Their removal can, at certain instants, reduce redundancy in the observation space and improve numerical conditioning, thereby marginally enhancing the filter’s performance in vorticity predictions. Interestingly, despite the simultaneous failure of 3 out of 11 sparse sensors (representing a 27% outage), the estimator maintains robust performance.

Overall, by examining how dominant observation modes evolve under sensor dropout, one can identify the relative importance of each sensor, assess redundancy in the sensing architecture, and quantify the robustness of the estimation framework to partial sensor failure. The findings confirm that the current approach maintains resilience to non-critical sensor loss, with minimal degradation in flow estimation accuracy. Even in the case of dropping a highly informative sensor—such as sensor 6 near the LE—the estimator adapts by reallocating observational weight to neighboring sensors and continues to perform well in predicting global quantities like lift and capturing the dominant large-scale vortical structures in the flow. Although posterior uncertainty increases and local flow features near the gust core and wake become less precisely reconstructed, the overall aerodynamic response remains accurately captured. This highlights the robustness of the learned filtering framework and its potential for real-time deployment in scenarios with limited or partially compromised sensing.

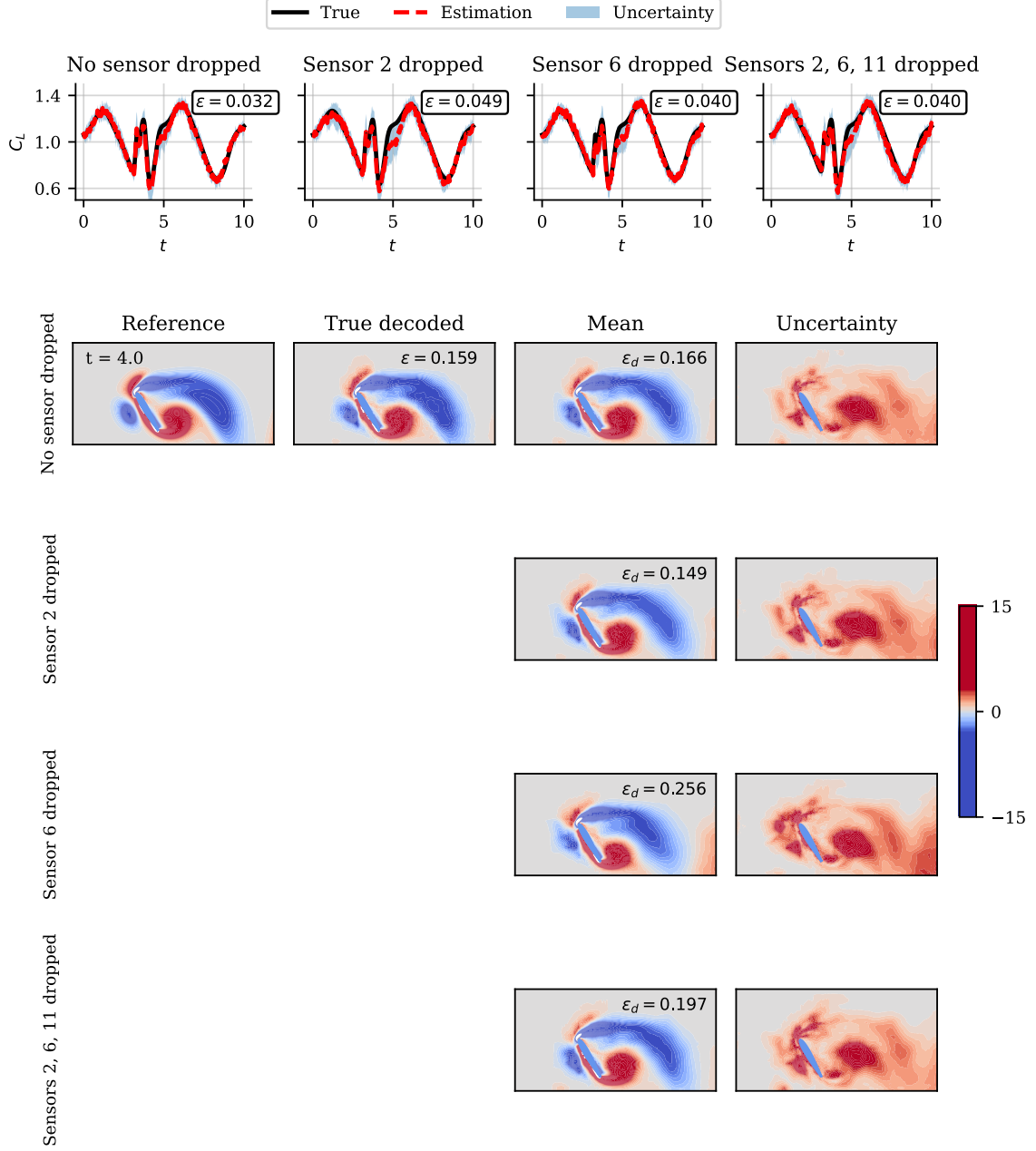


Figure 15: Effect of individual sensor dropout on the reconstructed lift (first panel) and vorticity fields (second to fourth panels) for the case ($\alpha = 60^\circ$, $D_y = -0.71$, $\sigma = 0.12$, $y_o = -0.19$, $t_o = 3.3$).

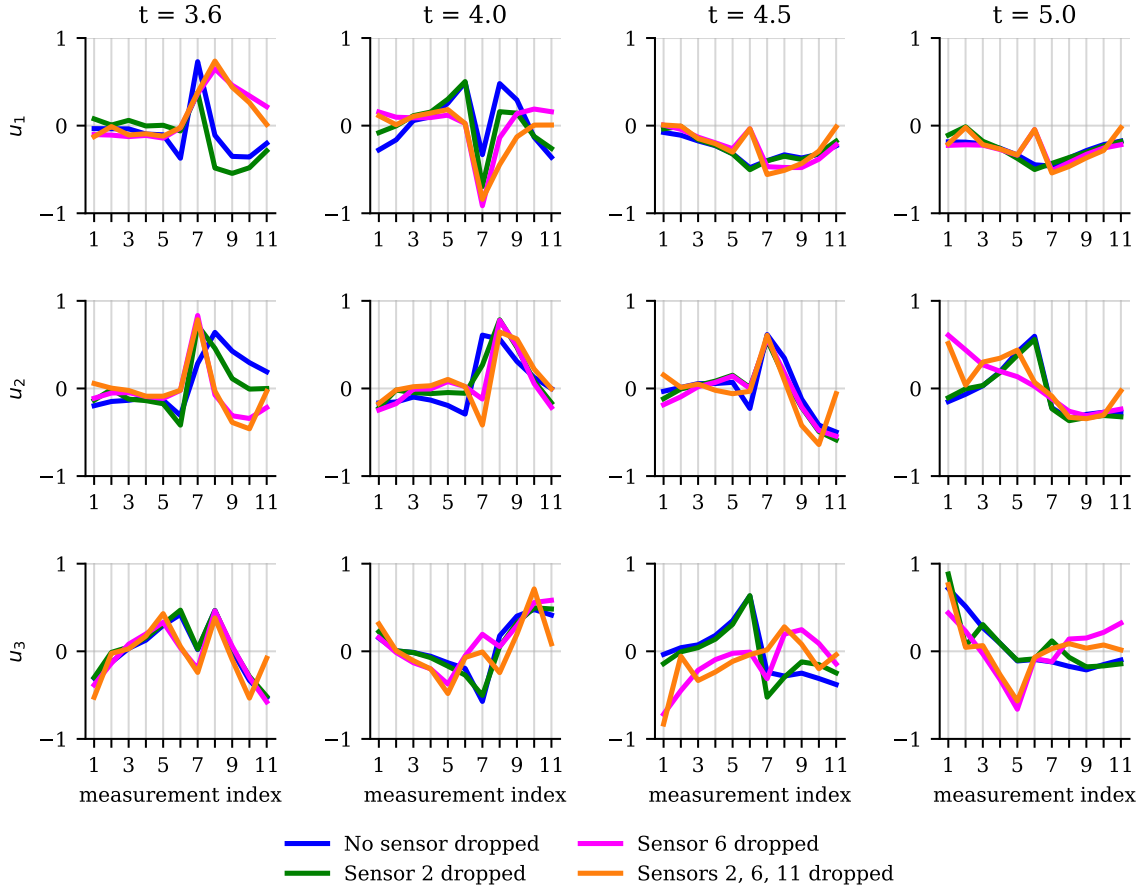


Figure 16: Effect of individual sensor dropout on the observation modes consistent with figure 15 at four representative time instances during the gust interaction. The condition is ($\alpha = 60^\circ$, $D_y = -0.71$, $\sigma = 0.12$, $y_o = -0.19$, $t_o = 3.3$).

3.4 Sequential estimation for an extrapolated case

All training and test aerodynamic cases discussed thus far involved disturbances introduced during the first vortex shedding cycle. To evaluate the robustness and generalizability of the estimator, it is critical to test its performance under extrapolative conditions—specifically when a disturbance occurs at an unseen phase of the shedding cycle. For this purpose, we construct a test case where a dipole-like gust is introduced at $t_o = 7$, well into the second shedding cycle, at the maximum AoA considered in this study, $\alpha = 60^\circ$. We refer to this as the extrapolation case. The results are presented in figure 17, showing the predicted lift coefficient and vorticity fields at three representative time instances during the gust–airfoil interaction. Before the gust enters the domain, the predicted lift trajectory matches the undisturbed periodic behavior with excellent accuracy, reflecting the estimator’s ability to maintain nominal performance under regular flow conditions. Remarkably, once the gust is introduced at $t_o = 7$, the pressure sensors immediately detect the upstream disturbance, resulting in a clear deviation from the undisturbed lift trajectory. This reflects the pressure field’s sensitivity to flow perturbations, even before their direct interaction with the airfoil around $t = 7.4$. Importantly, since the forecast operator was trained only on post-disturbance dynamics, it cannot anticipate the effect of an incoming gust at $t_o = 7$. As such, the forecasted latent states $\xi(t_o + \Delta t|t_o)$ remain confined to the undisturbed latent manifold. The deviation from undisturbed behavior is therefore initiated entirely by the correction introduced in the analysis step of filtering, wherein the discrepancy between observed and predicted pressures triggers an adjustment to the predicted states, resulting in the updated posterior $\xi(t_o + \Delta t|t_o + \Delta t)$.

The reconstructed vorticity field reflects this behavior. The posterior mean closely captures the dominant shear layers and large-scale vortices in regions near the sensors. The temporal evolution of the flow is accurately tracked, including the unsteady shedding patterns and the influence of the gust. Notably, the estimated uncertainty fields highlight elevated variance in key regions: the gust core, the near-wake shear layers, and along the outer boundaries of the separated flow structures. These regions coincide with areas less directly impactful on pressure observations, indicating that the filter correctly expresses confidence where data is informative and uncertainty where it is not. This extrapolation test confirms that the filtering framework generalizes well beyond its training window, relying on pressure-based corrections to capture flow disturbances introduced at unseen phases. The pressure sensors effectively detect and drive state corrections in real time, while the uncertainty quantification provides meaningful confidence estimates. This underscores the estimator’s reliability and adaptability in operational settings where disturbances may arise unpredictably.

One striking and consistent phenomenon observed across all estimated cases in Figures 9, 10, and 17 (as mentioned earlier) is the transient lift amplification caused by the interaction between the positive lobe of the dipole gust and the primary negative LE vortex. This interaction locally increases the effective angle of attack and momentarily elevates the lift coefficient. Shortly thereafter, the negative lobe of the dipole impinges on the airfoil, leading to a sharp decrease in lift. Notably, the largest estimation error and the highest uncertainty magnitude consistently occur during the time of maximum lift deviation from the undisturbed trajectory—precisely when the dipole is in closest interaction with the LE vortex. This phase corresponds to the most dynamically complex portion of the flow evolution, characterized by intense vortex interactions, rapid structural changes in the shear layer, and strong nonlinearity in the pressure response. The estimator reflects this complexity by exhibiting both increased prediction error and broader uncertainty bounds, indicating reduced observability and greater difficulty in capturing the rapidly changing flow state.

These demonstrations collectively highlight the capability of the proposed framework to transform sparse, noisy surface pressure measurements into reliable, uncertainty-aware reconstructions of high-dimensional flow fields in real time. By embedding neural-network surrogates within a low-rank ensemble filtering architecture, the method not only achieves computational efficiency but also adapts naturally to degraded sensing and extrapolative flow conditions. The result is an estimator that remains robust under severe disturbances, provides interpretable uncertainty quantification tied to observability, and scales efficiently for online deployment. Such capabilities establish a foundation for practical integration of flow state monitoring with feedback control and decision-making in unsteady aerodynamic environments.

4 Conclusion

This work proposed a data assimilation framework in a reduced space for real-time flow and load estimation in highly disturbed aerodynamic environments. By combining nonlinear autoencoders for compact state representation, neural-network-based surrogate models for dynamics and observations, and a low-

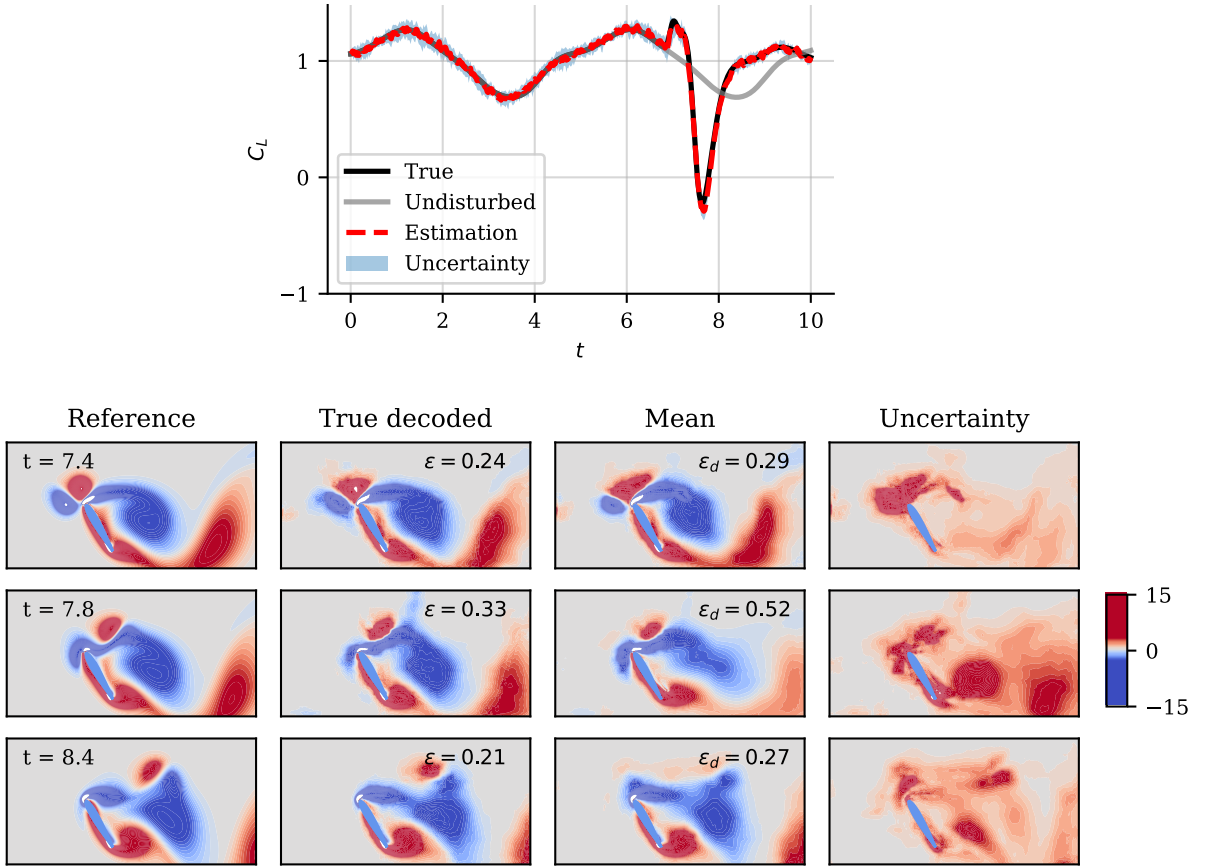


Figure 17: Estimated lift and vorticity field for disturbed aerodynamics at the extrapolation condition of ($\alpha = 60^\circ$, $D_y = -1.93$, $\sigma = 0.1$, $y_o = 0.22$, $t_o = 7.0$). The predicted ensemble mean along with the 95% confidence interval is shown for the lift coefficient and the vorticity field.

rank Ensemble Kalman Filter (LREnKF), the proposed approach enables accurate, uncertainty-aware estimation of unsteady flow fields from sparse, noisy surface pressure measurements. The estimator was evaluated across a wide range of gust-disturbed aerodynamic scenarios, including both interpolative cases—where disturbances occurred during the first vortex shedding cycle, consistent with training—and extrapolative cases—where gusts were introduced at arbitrary instants across the shedding cycle. In all test scenarios, the predicted lift closely followed the true unsteady dynamics, and the reconstructed vorticity fields accurately captured the dominant shear layers and vortical structures, especially in regions adjacent to sensor locations. The estimator demonstrated strong generalization capabilities, reliably tracking complex flow behavior under conditions not encountered during training.

To understand the limits of observability and estimation quality, the LREnKF was adopted to carry out state updates along the dominant directions of state and observation spaces. In all cases, the system was found to be effectively low-rank in the latent space, with only a few dominant latent directions being well-informed by the pressure observations. Similarly, a small number of observation directions—corresponding to linear combinations of sensor signals—were sufficient to capture most of the flow information. These findings highlight the underlying compression of the disturbed aerodynamic states and the selectivity of the sensors in constraining them. We further analyzed sensor informativeness over time by computing the dominant modes of the observation Gramian, which revealed the transient sensitivity of each pressure sensor to the evolving latent state. Leading-edge sensors were consistently the most informative, especially during gust–vortex interactions, while suction-side sensors near the trailing edge contributed less throughout the flow evolution. Sensor informativeness during gust encounters strongly depends on the gust structure. For example, in our previous work (Mousavi and Eldredge 2025), a Taylor gust produced a more disruptive interaction, leading to different information content across sensors compared to the less disruptive and more compact Gaussian gust considered in this study. It is important to note that the LREnKF employed in this study assumes all sources of uncertainty to be Gaussian or well-approximated as such. Nonetheless, for strongly nonlinear and non-Gaussian systems, this framework can be extended using the gradient-based Gramian estimation approach proposed by Baptista et al. (2022).

In addition, we investigated the role of unobservable latent directions, i.e., directions in the latent space that lie in the nullspace of the gradient of the learned observation operator. Perturbations along these directions do not affect the predicted pressure observations but can still propagate through the decoder to influence the reconstructed vorticity field. This highlights a subtle but important limitation: although the filter cannot constrain these directions directly, their physical effect manifests in downstream flow quantities, potentially contributing to persistent uncertainty or bias in regions remote from or less informed by sensors. These unobservable latent directions also impact the estimator’s performance during the post-disturbance period, when the gust has convected downstream of the airfoil and the flow returns to its undisturbed state. In this interval, the estimator occasionally interprets residual uncertainties as spurious upstream gusts, resulting in artificially elevated uncertainty in regions where no actual disturbance exists.

To probe the estimator’s robustness, we studied the impact of sensor dropout by artificially increasing the uncertainty of key sensors, effectively removing them from the assimilation process. Remarkably, even when the most informative leading-edge sensor was dropped, the estimator maintained high accuracy. This resilience stems from the low-rank structure of the system: when a dominant sensor is lost, the filter implicitly increases the Kalman gain weights on neighboring sensors, allowing them to compensate and reconstruct the dominant flow features. As a result, the degradation in lift and vorticity estimation was minimal, confirming that the estimator leverages spatial redundancy and shared observability among nearby sensors.

A key and consistent phenomenon observed across all test cases was the aerodynamic response to dipole gusts. When the positive lobe of the dipole interacted with the primary negative leading-edge vortex, it transiently increased the effective angle of attack, producing a sharp lift surge. This was followed by a rapid lift drop caused by the arrival of the negative lobe, which disrupted the vortex structure. These gust–vortex interactions corresponded to the most dynamically complex phases of the flow evolution and were consistently associated with the largest estimation errors and highest posterior uncertainty. The uncertainty fields correctly identified regions of limited observability—such as the gust core and wake shear layers—indicating that the estimator not only reconstructs the dominant flow features but also provides reliable confidence bounds.

Overall, the results demonstrate that the proposed framework achieves accurate and efficient flow state estimation under strong disturbances, with robustness to sensor dropout and generalization to unseen gust realizations. By exploiting low-rank structure and integrating uncertainty quantification, this

method provides a scalable and reliable foundation for flow monitoring, feedback control, and decision-making in real-time aerodynamic systems where traditional solvers are computationally prohibitive.

A critical component in bridging sparse pressure observations with high-dimensional flow state estimation is the construction of a low-dimensional latent representation. However, as discussed in this study, the resulting latent space lacks clear physical interpretability, making it challenging to relate individual latent components to specific flow structures or phenomena. Future work may focus on enhancing interpretability—either through targeted regularization strategies or by modifying the autoencoder architecture—to promote more physically meaningful latent variables and improve transparency in the estimation process. It should be emphasized that this study explored an extreme scenario in which the forecast operator lacks long-time accuracy, demonstrating that even under such conditions, surface pressure measurements contain sufficient flow information to effectively correct the predicted states through filtering. However, the limitations imposed by unobservable latent directions—those that cannot be recovered from pressure data alone—can be mitigated by learning a more accurate forecast operator, which provides a stronger prior for the filtering process. As stated in our discussions before, incorporating history-aware models such as Recurrent Neural Networks (RNNs) significantly enhances the temporal prediction of latent states. While this approach departs from the classical Markovian assumption typically required in sequential filtering, filters like the EnKF can still be applied in weakly or non-Markovian settings. In such cases, although we would sacrifice the strict mathematical optimality of the Kalman update, the improved forecast model can compensate by providing richer dynamics and reducing reliance on measurement correction alone. Nonetheless, these memory-based approaches should be adopted with caution, particularly when interpretability and theoretical guarantees are important. Finally, this framework is broadly applicable to systems where a reduced-order state representation can be constructed.

Acknowledgments

The authors gratefully acknowledge the financial support provided by the National Science Foundation under award numbers 2247005 and 2247006.

References

- Asch, M., Bocquet, M., and Nodet, M. (2016). *Data Assimilation: Methods, Algorithms, and Applications*. SIAM.
- Bach, E., Baptista, R., Sanz-Alonso, D., and Stuart, A. (2024). Inverse Problems and Data Assimilation: A Machine Learning Approach. *arXiv preprint arXiv:2410.10523*.
- Baptista, R., Marzouk, Y., and Zahm, O. (2022). Gradient-based data and parameter dimension reduction for Bayesian models: an information theoretic perspective. *arXiv preprint arXiv:2207.08670*.
- Berkooz, G., Holmes, P., and Lumley, J. L. (1993). The proper orthogonal decomposition in the analysis of turbulent flows. *Annual review of fluid mechanics*, 25(1):539–575.
- Cheng, S., Prentice, I. C., Huang, Y., Jin, Y., Guo, Y.-K., and Arcucci, R. (2022). Data-driven surrogate model with latent data assimilation: Application to wildfire forecasting. *Journal of Computational Physics*, 464:111302.
- Coskun, H., Achilles, F., DiPietro, R., Navab, N., and Tombari, F. (2017). Long short-term memory kalman filters: Recurrent neural estimators for pose regularization. In *Proceedings of the IEEE International Conference on Computer Vision*, pages 5524–5532.
- Cui, T. and Zahm, O. (2021). Data-free likelihood-informed dimension reduction of Bayesian inverse problems. *Inverse Problems*, 37(4):045009.
- da Silva, A. F. and Colonius, T. (2018). Ensemble-based state estimator for aerodynamic flows. *AIAA Journal*, 56(7):2568–2578.
- de Rosnay, P., Browne, P., de Boissés, E., Fairbairn, D., Hirahara, Y., Ochi, K., Schepers, D., Weston, P., Zuo, H., Alonso-Balmaseda, M., et al. (2022). Coupled data assimilation at ECMWF: current status, challenges and future developments. *Quarterly Journal of the Royal Meteorological Society*, 148(747):2672–2702.

- Eldredge, J. D. (2022). A method of immersed layers on Cartesian grids, with application to incompressible flows. *Journal of Computational Physics*, 448:110716.
- Eldredge, J. D. and Mousavi, H. (2025). A review of Bayesian sensor-based estimation and uncertainty quantification of aerodynamic flows. *arXiv preprint arXiv:2502.20280*.
- Evensen, G. (1994). Sequential data assimilation with a nonlinear quasi-geostrophic model using Monte Carlo methods to forecast error statistics. *Journal of Geophysical Research: Oceans*, 99(C5):10143–10162.
- Fraccaro, M., Kamronn, S., Paquet, U., and Winther, O. (2017). A disentangled recognition and nonlinear dynamics model for unsupervised learning. *Advances in neural information processing systems*, 30.
- Fukami, K., Smith, L., and Taira, K. (2025). Extreme vortex-gust airfoil interactions at reynolds number 5000. *Physical Review Fluids*.
- Fukami, K. and Taira, K. (2023). Grasping extreme aerodynamics on a low-dimensional manifold. *Nature Communications*, 14(1):6480.
- Ghosh, A., Eldar, Y. C., and Chatterjee, S. (2024a). Data-driven Bayesian State Estimation with Compressed Measurement of Model-free Process using Semi-supervised Learning. *arXiv preprint arXiv:2407.07368*.
- Ghosh, A., Honoré, A., and Chatterjee, S. (2024b). DANSE: Data-driven non-linear state estimation of model-free process in unsupervised learning setup. *IEEE transactions on signal processing*.
- He, X., Tran, A., Bortz, D. M., and Choi, Y. (2025). Physics-Informed Active Learning With Simultaneous Weak-Form Latent Space Dynamics Identification. *International Journal for Numerical Methods in Engineering*, 126(1):e7634.
- Howard, L. J., Subramanian, A., and Hoteit, I. (2024). A machine learning augmented data assimilation method for high-resolution observations. *Journal of Advances in Modeling Earth Systems*, 16(1):e2023MS003774.
- Jin, X.-B., Robert Jeremiah, R. J., Su, T.-L., Bai, Y.-T., and Kong, J.-L. (2021). The new trend of state estimation: From model-driven to hybrid-driven methods. *Sensors*, 21(6):2085.
- Jouaber, S., Bonnabel, S., Velasco-Forero, S., and Pilte, M. (2021). NNAKF: A neural network adapted Kalman filter for target tracking. In *ICASSP 2021-2021 IEEE International Conference on Acoustics, Speech and Signal Processing (ICASSP)*, pages 4075–4079. IEEE.
- Kalnay, E. (2003). *Atmospheric modeling, data assimilation and predictability*. Cambridge university press.
- Le Dimet, F.-X. and Talagrand, O. (1986). Variational algorithms for analysis and assimilation of meteorological observations: theoretical aspects. *Tellus A: Dynamic Meteorology and Oceanography*, 38(2):97–110.
- Le Provost, M., Baptista, R., Marzouk, Y., and Eldredge, J. (2021). A low-rank nonlinear ensemble filter for vortex models of aerodynamic flows. In *AIAA Scitech 2021 Forum*, page 1937.
- Le Provost, M., Baptista, R., Marzouk, Y., and Eldredge, J. D. (2022). A low-rank ensemble Kalman filter for elliptic observations. *Proceedings of the Royal Society A*, 478(2266):20220182.
- Le Provost, M. and Eldredge, J. D. (2021). Ensemble Kalman filter for vortex models of disturbed aerodynamic flows. *Physical Review Fluids*, 6(5):050506.
- Maulik, R., Mohan, A., Lusch, B., Madireddy, S., Balaprakash, P., and Livescu, D. (2020). Time-series learning of latent-space dynamics for reduced-order model closure. *Physica D: Nonlinear Phenomena*, 405:132368.
- Maybeck, P. S. (1982). *Stochastic models, estimation, and control*, volume 3. Academic press.
- Moldovan, G., Lehnasch, G., Cordier, L., and Meldi, M. (2021). A multigrid/ensemble Kalman filter strategy for assimilation of unsteady flows. *Journal of Computational Physics*, 443:110481.

- Mori, H. (1965). Transport, collective motion, and Brownian motion. *Progress of theoretical physics*, 33(3):423–455.
- Mousavi, H. and Eldredge, J. D. (2025). Low-Order Flow Reconstruction and Uncertainty Quantification in Disturbed Aerodynamics Using Sparse Pressure Measurements. *Journal of Fluid Mechanics*, 1013:A41.
- Özalp, E., Nóvoa, A., and Magri, L. (2025). Real-time forecasting of chaotic dynamics from sparse data and autoencoders. *arXiv preprint arXiv:2508.08729*.
- Popov, A. A. and Sandu, A. (2022). Multifidelity ensemble Kalman filtering using surrogate models defined by theory-guided autoencoders. *Frontiers in Applied Mathematics and Statistics*, 8:904687.
- Revach, G., Shlezinger, N., Ni, X., Escoriza, A. L., Van Sloun, R. J., and Eldar, Y. C. (2022). KalmanNet: Neural network aided Kalman filtering for partially known dynamics. *IEEE Transactions on Signal Processing*, 70:1532–1547.
- Ruiz, R. B., Marwah, T., Gu, A., and Risteski, A. (2024). On the Benefits of Memory for Modeling Time-Dependent PDEs. *arXiv preprint arXiv:2409.02313*.
- Schmid, P. J. (2010). Dynamic mode decomposition of numerical and experimental data. *Journal of fluid mechanics*, 656:5–28.
- Smith, L., Fukami, K., Sedky, G., Jones, A., and Taira, K. (2024). A cyclic perspective on transient gust encounters through the lens of persistent homology. *Journal of Fluid Mechanics*, 980:A18.
- Song, F., Li, Y., Cheng, W., Dong, L., Li, M., and Li, J. (2022). An Improved Kalman Filter Based on Long Short-Memory Recurrent Neural Network for Nonlinear Radar Target Tracking. *Wireless Communications and Mobile Computing*, 2022(1):8280428.
- Tang, M., Liu, Y., and Durlofsky, L. J. (2020). A deep-learning-based surrogate model for data assimilation in dynamic subsurface flow problems. *Journal of Computational Physics*, 413:109456.
- Wang, R. and Shen, Z. (2024). A Deep Neural Network-Ensemble Adjustment Kalman Filter and Its Application on Strongly Coupled Data Assimilation. *Journal of Marine Science and Engineering*, 12(1):108.
- Xie, X., Mowlavi, S., and Benosman, M. (2024). Smooth and Sparse Latent Dynamics in Operator Learning with Jerk Regularization. *arXiv preprint arXiv:2402.15636*.
- Zwanzig, R. (1961). Memory effects in irreversible thermodynamics. *Physical Review*, 124(4):983.